February 2021

A Feedback-Based Pneumatic Compression System for Effective Lymphedema Management

Mohammad Imrul Kayes

A FEEDBACK-BASED PNEUMATIC COMPRESSION SYSTEM FOR EFFECTIVE LYMPHEDEMA MANAGEMENT

A Thesis

Submitted to the Graduate Faculty of the
Louisiana State University and
Agricultural and Mechanical College
in partial fulfillment of the
requirements for the degree of
Master of Science in Mechanical Engineering

in

The Department of Mechanical and Industrial Engineering

by
Mohammad Imrul Kayes
M.S. Mechanical Engineering, Louisiana Tech University, 2017
May 2021

BRUNO

ACKNOWLEDGMENTS

On this day, I would like to remember all my ancestors who came before me, hunted in groups for food, and domesticated dogs. I would like to thank Bruno for coming into my life and making it beautiful without uttering a single word. I am grateful to Dr. Carl Sagan for being an inspiration in my life. I am thankful to my best friend and wife Meghla for being there when I needed her. I would also like to thank my parents for deciding to get married, give birth to me, and raise me.

I am grateful to my supervisor Dr. Hunter Gilbert for his continuous support, positive reinforcement, and patience. There were times when I faced challenges and difficulties, and Dr. Gilbert was always there to help me overcome those. I appreciate the suggestions and feedback from Mrs. Connie McKnight, who also helped with the initial design concept for the work. I would also like to thank Dr. Corina Barbalata and Dr. Marcio de Queiroz for providing me guidance from time to time. I am thankful to all the members of ICORE lab, especially Tonmoy and Parsa for helping me debug codes, and discussing with me about life.

I want to thank all the members of Tiger Cricket Club at LSU for making my weekends wonderful. I have had some beautiful memories with my fellow teammates and hopefully this will continue.

Last but not the least, I would like to thank all the janitors, maintenance staffs, electricians, plumbers, and other essential workers at Patrick F Taylor Hall who work hard to make sure we excel at what we do. Thank you!

TABLE OF CONTENTS

ACKNOWLEDGMENTS iii

ABSTRACT vi

CHAPTER 1. INTRODUCTION 1
1.1. Lymphatic System 2
1.2. Types of Lymphedema 4
1.3. Lymphedema Measurements 5
1.4. Lymphedema Treatments 6
1.5. Design Requirements 8
1.6. Problem Statement 9
1.7. Research Objectives 9
1.8. Experimental Approach 11

CHAPTER 2. MATERIALS AND METHODS 13
2.1. Modeling The Lymphatic System 13
2.2. Design of Compression Subsystem 18
2.3. Design of BIA Subsystem 20
2.4. Calculation of Battery Life and Number of Compression Cycles 31

CHAPTER 3. RESULTS AND ANALYSIS 33
3.1. Lymphatic System 33
3.2. Compression Subsystem 35
3.3. BIA Subsystem 37
3.4. Battery Life and Number of Compression Cycles 46

CHAPTER 4. DISCUSSION 48
4.1. Lymphatic System 48
4.2. Compression Subsystem 48
4.3. BIA Subsystem 49
4.4. Battery Life and Portability 50

CHAPTER 5. CONCLUSION 52

CHAPTER 6. FUTURE WORK 54

APPENDIX A. SIMULINK MODEL FOR LYMPHANGION CHAIN NETWORK 56

APPENDIX B. ARDUINO CODE FOR SEQUENTIAL OPERATION OF PUMPS 57

APPENDIX C. ARDUINO CODE FOR SINGLE FREQUENCY IMPEDANCE MEASUREMENT 58

REFERENCES 62

VITA 66

ABSTRACT

Bioimpedance analysis (BIA) is a method of detecting lymphedema- a debilitating medical condition involving swelling of the extremities. Pneumatic compression devices are frequently used in the compression treatment of lymphedema. Although existing compression technology provides relief of symptoms, it has limitations in terms of ease-of-use, portability, and monitoring of treatment progress. Currently, there are no BIA analyzers in the market that run on a low-power microcontroller and a rechargeable battery. Moreover, no such device currently exists that integrate the BIA analysis with pneumatic compression system to offer a feedback-based solution for lymphedema treatment. This work represents the first steps towards a complete system and describes the pneumatic compression and circuit designs for a portable BIA analyzer. The study proposes a lightweight, battery operated pneumatic compression device that can apply a pressure of 50 mmHg in a four-chamber compression garment. A microcontroller-based BIA system that can provide accurate indication of swelling based on a Nyquist plot was introduced. The envisioned mechatronic system features programmable compression sequences and operates with the human-in-the-loop using bioimpedance spectroscopy as control feedback. Performance of the compression system is verified by measurement of applied pressures and the BIA circuits are validated for single frequency and multi frequency impedance analysis of a phantom test load. With further development in the future, the system has the potential to serve as a quantitative source of valuable diagnostic information for clinicians, and in the long run may enable the smart management of lymphedema with the device essentially prescribing the course of treatment in response to measured conditions. This kind of human-in-the-loop control system may be a breakthrough in treatment of chronic conditions.

CHAPTER 1. INTRODUCTION

Lymphedema is a condition (or set of conditions) where excessive interstitial protein-rich fluid is accumulated in particular limb(s) of the body [1]. It occurs when there is an imbalance between the lymphatic flow and lymphatic circulation. In other words, when the lymphatic system cannot provide enough circulation of lymphatic flow, the affected limb(s) can suffer from chronic conditions like swelling, aching, heaviness, and impaired freedom of movement, Figure 1.1. Additionally, skin infections such as cellulitis are common in lymphedema.

Figure 1.1. Schematic of a typical case of lymphedema- causing swelling in the right arm.

In addition to swelling and other associated discomforts, lymphedema can greatly affect quality of life and the perception of well-being [2]. Several psychological issues such as depression, anxiety, and isolation are manifested by patients with lymphedema [3]–[5]. Studies suggest that women suffering from breast cancer related lymphedema showed less compliance with available treatments due to those psychological factors [4], [5].

1.1. LYMPHATIC SYSTEM

To understand lymphedema, it is important to understand the lymphatic system in the body. The lymphatic system is a large network of lymph vessels, lymphoid tissues, and a circulating clear fluid called 'lymph'. The lymphatic system removes excess fluid and waste from the body tissues and returns it to the bloodstream. It also helps to absorb fat and fat-soluble vitamins from the digestive system. The primary function of the lymph vessels is to carry the lymph throughout the body, Figure 1.2.

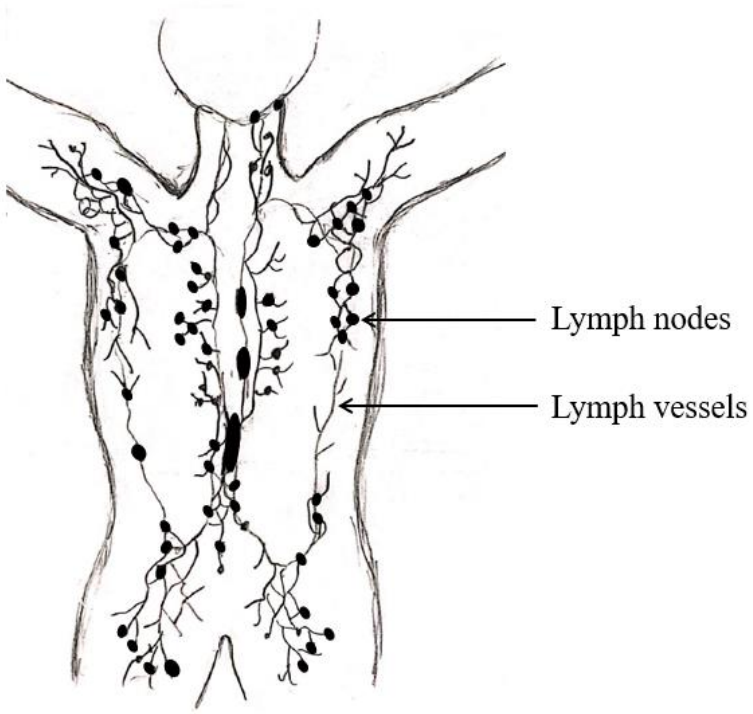

(a) Schematic of distribution of lymph nodes in the upper extremity.

(figure cont'd)

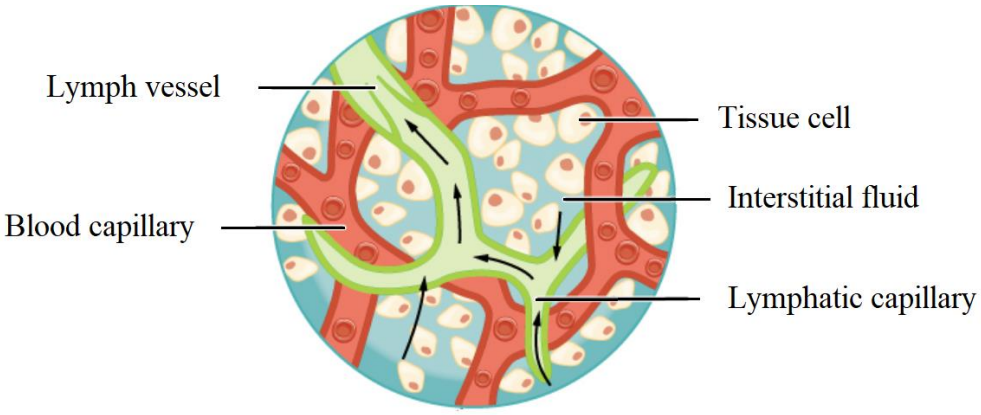

(b) Structure of a lymph node (Courtesy of OpenStax College 2014) [6] .

Figure 1.2. The lymphatic system of a human body.

Lymph contains waste products and cellular debris that need to be filtered from bloodstream [7]. A large number of lymph nodes (around 500-600) distributed throughout the body by lymphatic vessels act as a filter for these waste products and debris. If there are signs of an infection, the body makes excess lymphocytes (white blood cells) to fight that infection. When the number of lymphocytes increases, the lyph nodes along the lymph vessels that drain the infected area swell. A typical example would be an infection in the throat that causes the lymph nodes in the neck to swell.

The functional units of a lymphatic vessel is called lymphangions. They are nestled between two lymph valves and play a major role in pumping lymph fluid by cyclically contracting and relaxing the lymphatic muscles Figure 1.3. The amount of lymph fluid pumped by lymphangions is governed by factors like lymphangion length, contraction frequency of lymphatic muscles, and external pressure [8]. The lymph valves are directed toward the direction of lymph flow as seen in Figure 1.3.

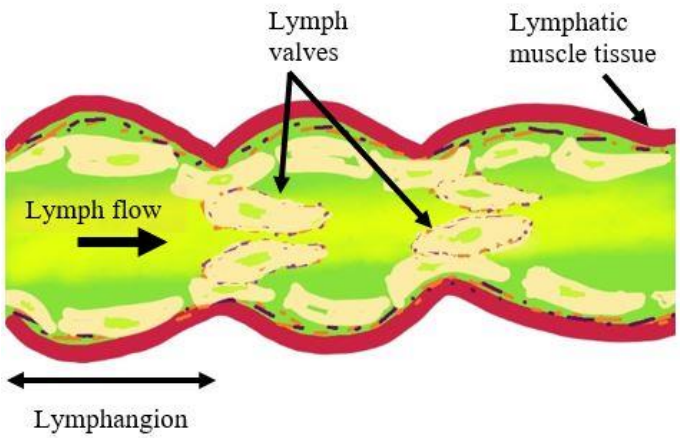

Figure 1.3. Schematic of a lymphangion chain network.

In an effectively working lymphatic system, the valves open when the pressure in the first lymphangion is higher than in the next lymphangion. Once the lymph flows to the next lymphangion, the valve closes tightly, hence allowing only a unidirectional flow. In the case of lymphedema, the pressure in a lymphatic system is much higher than a normal lymphatic system due to the excess interstitial fluid. As a result, the lymphatic valves fail to function properly and the unidirectional lymph flow gets disrupted. This results in a much lower outflow of lymph fluid from the system- an indication of lymphedema.

1.2. TYPES OF LYMPHEDEMA

Lymphedema can be classified as primary and secondary. Primary lymphedema is a rare and inherited condition caused by defective lymph vessels in the body. Secondary lymphedema, which is more common than the primary form, is caused by disruption of lymphatic pathways as a consequence of a surgery that typically involves removal of lymph nodes [9]. When lymphatic tissues or lymph nodes are removed, the lymph cannot be drained efficiently from the affected area. As a consequence, excess lymph accumulates and causes swelling.

In the last 45 years, the global occurrence of secondary lymphedema has increased by 4 times [1], [10]. In USA, nearly 1 in every 1000 people are suffering from secondary lymphedema, Figure 1.4. Lymphedema can occur in both the upper and the lower extremities of the body. In the USA, the most common form of secondary lymphedema is the edema of the arm. Typically this is caused by axillary lymph node (around the armpit) dissection as a part of breast cancer surgery [11]. The incidence of lymphedema after breast cancer surgery may be as high as 70% [12].

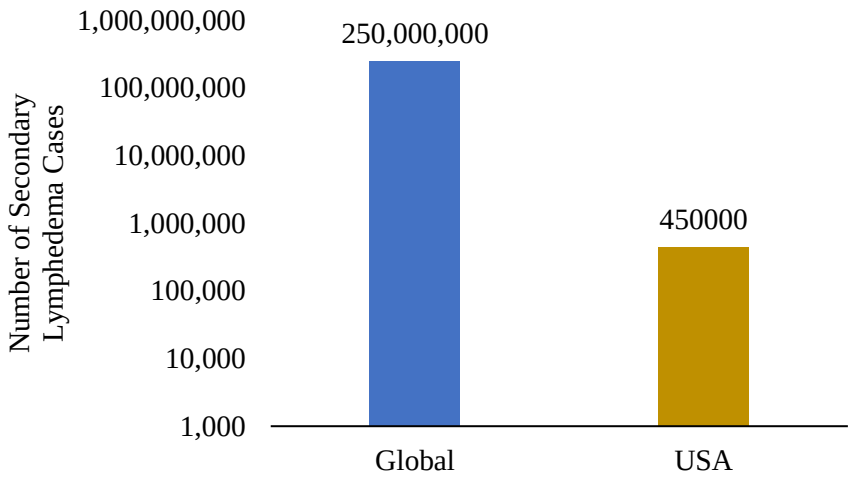

Figure 1.4. Number of secondary lymphedema cases- Global vs USA.

1.3. LYMPHEDEMA MEASUREMENTS

For the measurement of lymphedema, a non-invasive technique called bio impedance analysis (BIA) is used to monitor changes in total body water (TBW), extra-cellular fluid (ECF), intra-cellular fluid (ICF), fat mass, and fat free mass. By sending a low-level AC current through the body, the resistance and reactance are measured. At very low frequency, the current cannot pass throught the cell walls, allowing the measurements of only extra-cellular fluid (ECF) impedance, Figure 1.5. Conversely, at very high frequencies, the current can pass through the

cell walls, allowing the measurements of total body water (TBW) impedance. The intra-cellular fluid (ICF) impedance can be obtained by subtracting the ECF impedance from the TBW impedance. Furthermore, the ECF and ICF impedance can be used to calculate fat mass and fat-free mass.

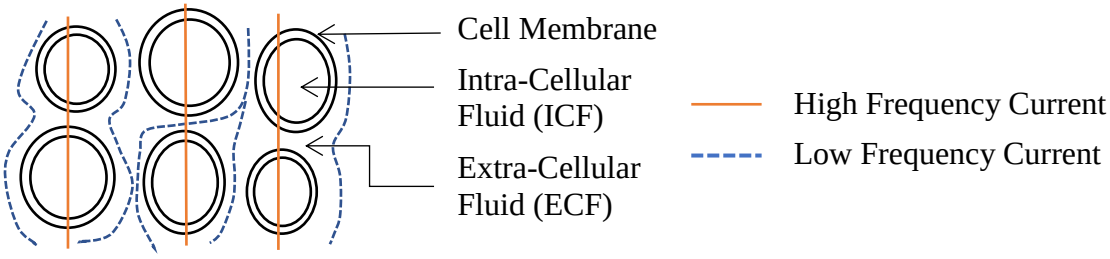

Figure 1.5. Low and high frequency current flow in body cells.

Bio impedance spectroscopy (BIS) analysis is the most advanced form of BIA which measures fluid and tissue volume that gives an accurate indication of lymphedema. The technique is capable of detecting lymphedema symptoms by measuring the change in ECF in the body [13]. Typically, a Nyquist plot of the body component's electrical transfer function is obtained by plotting real and imaginary impedance (ex. resistance and reactance) of the body for a sweep of test frequencies. A mixture model of the tissue indicates that quantities of extracellular water and total water correspond to impedance measured at a very low (zero) frequency and a very high (infinite) frequency, respectively [14].

1.4. Lymphedema Treatments

Lymphedema is a chronic condition that needs continuous and meticulous care. Complete decongestive physiotherapy (CDP) is an effective option for the initial treatment of lymphedema. The treatment includes manual lymphatic drainage (MLD), compression stockings and bandages, and pneumatic compression [15]. Study suggests that patients who showed compliance with

CDP had an average reduction of 59% in upper extremity volume on a 9 month follow-up [16]. However, CDP involves care by a trained specialist in a clinical setting and therefore it cannot be sustained forever. Patients must eventually transition into self-care in an at-home setting [17].

Use of compression devices as a part of CDP showed reduced limb volume and improved lymphatic function [18], [19]. Recent guidelines suggest using pneumatic compression devices for 1 hour per day with maximum pressure ranging from 30 mmHg to 60 mmHg [19]. A typical pneumatic compression device consists of a compression garment having single or multiple chambers and a pneumatic pump, Figure 1.6. A multi-chamber compression garment allows calibrated gradient pressure in the chambers, targeting specific areas for compression [20]. The pneumatic pumps apply sequential pressure that varies along the length of the treatment area (upper or lower extremity) and over time, which is categorized as dynamic therapy. This kind of therapy is designed to stimulate fluid circulation through open channels and improve conditions for uptake of fluid into the lymphatics.

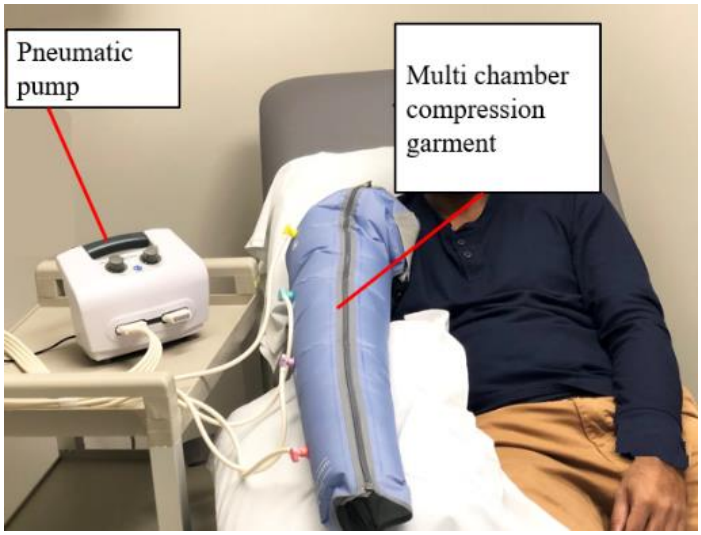

Figure 1.6. A traditional pneumatic compression device with a pneumatic pump and multi-chamber compression garment.

1.5. DESIGN REQUIREMENTS

The regular and compliant compression treatment for lymphedema requires a compression device that is able to apply sufficient pressure to cause movement of lymph fluid. A minimum of 30 mmHg pressure needs to be maintained by a prefabricated or custom-fabricated compression garment to be classified as a compression treatment device [21]. In case of a gradient pressure (from lowest to highest pressure point) the applied pressure needs to be sufficient to move lymph fluid from distal to proxima or vice versa. Additionally, no tourniquet effect should be observed at any point during the compression treatment. For inflation of a multichamber compression garment, the time of inflation needs to be sufficient for translocation of lymph fluid in proximal region [22]. A typical sequential pneumatic comression pump can weigh around 5 lbs with the applied pressure as high as 125 mmHg [23].

The compression garment should be designed such a way that prevents skin infection and allows as much freedom of movement as possible [24]. The garment should not be too tight and should be able to provide a firm support. A clinical decision-making is required to determine the firmness of the fabric on the skin of an individual. The garment should be able to withstand frequent washing, exposure to sun, and stretching from donning and doffing, and be able to provide effective compression for four to six months [25].

A BIA analysis device should be able to determine the following three pure resistances in the body [26]-

- Resistance at zero (very low) frequency that indicates free fluid outside of body cells
- Intra-cellular fluid (ICF) resistance that indicates intra-cellular fluid inside of body cells
- Resistance at infinite (very high) frequency that indicates total body water (TBW) including fluid inside of body cells

The range of frequency used for a BIS analysis can vary widely. However a wide frequency band (ex. 3 kHz to 1000 kHz) typically provides a more accurate information on tissue properties.

1.6. PROBLEM STATEMENT

There are a number of companies that manufacture pneumatic compression devices for lymphedema. Tactile medical and Bio Compression Systems Inc. are two of the major manufacturers of such products. The Flexitouch system provided by Tactile medical is based on the stimulation of lymphatic system that helps with lymphatic function improvement [27]. Bio Compression Systems Inc. manufactures compression pumps based on intended use such as primary and secondary lymphedema, and chronic venous stasis ulcers.

Although the intermittent pneumatic compression (IPC) shows a significant 12% reduction in swelling for upper extremity lymphedema [28], the current compression treatment options require patients to wear a bulky and uncomfortable compression garment and be tethered to a stationary pneumatic pump during the duration of the process. This can greatly interfere with the daily living of the patients. Moreover, no such device currently exists that couple the BIS analysis with compression devices to monitor treatment progress over time and provide feedback. Thus, the existing compression technology has limitations in terms of ease-of-use, portability, and monitoring of treatment progress.

1.7. RESEARCH OBJECTIVES

A feedback-based portable compression system that monitors the progress and adjust treatment courses may provide a better solution to lymphedema management. The use of a BIA system to regulate compression and treatment duration can substantially reduce the physical

concerns associated with this disease. A compression garment that is less obtrusive and easy to wear can provide greater comfort to the treatment and improve psychological and functional well-being of a person. The ability to quantify the condition can also provide substantial motivation for the user to comply with therapy, an effect associated with the idea of the "Quantified Self" [29]. The long-term benefit of such technology can provide a reduced risk of infection and chronic condition.

This research introduces the concept of a smart pneumatic system that provides dynamic compression therapy. As an initial approach, the work aimed at producing a simulation of lymphatic network system in the upper body. Once this was accomplished, the work focused on developing a light-weight, battery operated pneumatic compression device that can apply compression in an 'easy to wear' compression garment for upper extremity (arm) lymphedema. Another objective of current work was to propose a custom-designed BIA measurement system that can provide impedance measurements of a human arm in a battery-powered device. Finally, the research aimed at integrating the subsystems into a single unit to create a portable and convenient solution for lymphedema treatment.

This thesis has three main research objectives:

1. Produce a simulation model demonstrating the effect and mechanism of pumping action generated by external pressure variations applied to the lymphatic network.
2. Design and develop a light-weight, battery-operated pneumatic compression device that applies compression in an easy to wear garment for upper extremity (arm) lymphedema.
3. Design a custom, low-cost bioimpedance analysis measurement system to facilitate estimation of the swelling state of the upper arm in a portable, battery-powered device

aimed at supporting the future development of a feedback control system for treatment of lymphedema.

1.8. EXPERIMENTAL APPROACH

The general research approach to fulfill the objectives of this study is presented in Figure 1.7. An experimental program was developed for a compression subsystem and a BIA subsystem. The development of compression subsystem included the design and development of compression garment and pneumatic pumps. Once developed, the components of the compression subsystem were integrated and tested for sequential pneumatic compression. The development of BIA subsystem included the design of a test circuit for single frequency and multi frequency BIA measurements. The circuit performance was validated using a benchtop LCR meter. Finally, the findings from both subsystems were analyzed for discussion followed by recommendations for future work.

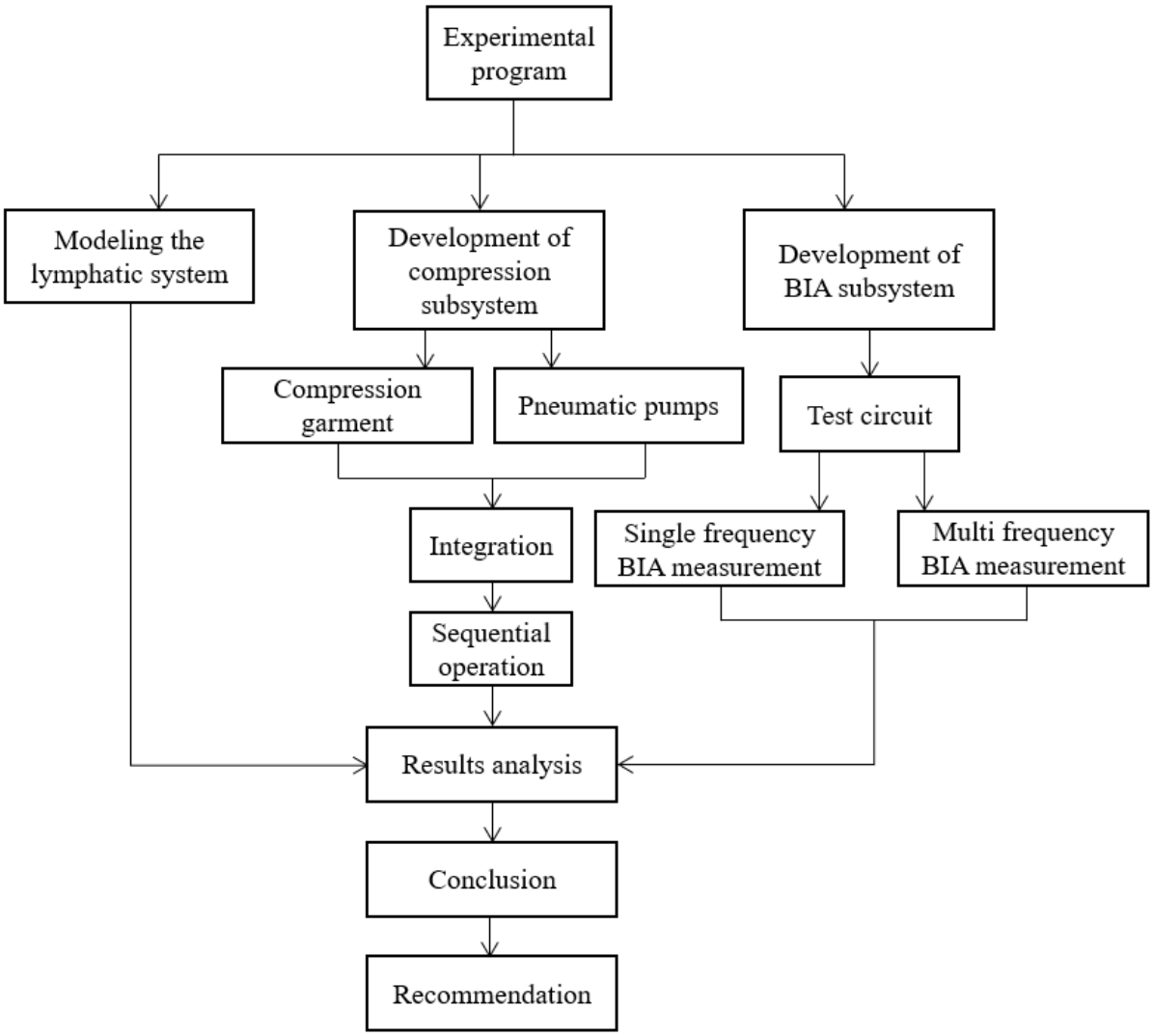

Figure 1.7. General layout of research approach.

CHAPTER 2. MATERIALS AND METHODS

2.1. MODELING THE LYMPHATIC SYSTEM

An early work on modeling the lymphatic system was performed by Reddy et al. in 1975 [30]. They presented a mathematical model of the whole-body lymphatic network that analyzed the characteristics of lymphatic contractility at various points. Drake et al. presented the equivalent circuit technique for lymph flow studies in 1986 [31]. They applied circuit analysis techniques to model and analyze the lymphatic systems. The equivalent circuit consisted of a single resistor in series with a single pressure source with the lymphatic valves represented by diodes.

To gain an understanding of the mechanisms of action by which external compression therapy may aid in the pumping of lymph and reduction of lymphedema-related swelling, we investigated the effect of external pressure modulations on an existing mathematical model of a lymphangion first presented by Bertram et al. [32]. The model is a lumped-parameter model which includes the effects of stretch in the lymphangion walls (fluid capacitance); the Hagen-Poiseuille resistance to flow due to fluid viscosity (linear fluid resistance); the nonlinear diode-like behavior of valves present in the lymphangion network (nonlinear fluid resistance); the active muscle contractions that normally exist in lymphangions (pressure sources); and the presence of varying fluid pressure at the ends of a lymphangion chain and in the vicinity of each lymphangion unit (pressure sources) [8]. The parameter lumping strategy associates the lymphangion body with two fluid resistance elements and a nonlinear capacitance combined with an active pressure source.

Four individual lymphangions were connected in series to create a branching network structure, Figure 2.1. A number of contractile vessel segments with diameter D_i linked by valves $(i = 1, 2, 3, 4)$ formed the series chain that began at a reservoir of a constant pressure p_a and ended at a higher pressure p_b. Each vessel segment was subject to an external pressure p_{ei} and gave rise to an inlet pressure p_{i1}, a midpoint pressure p_{im}, and an outlet pressure p_{i2}. With the pressure gradient across the vessel wall defined as the transmural pressure p_{tm}, the midpoint pressure p_{im} was obtained from the following equation-

$$p_{im} = p_{ei} + p_{tm} \tag{1}$$

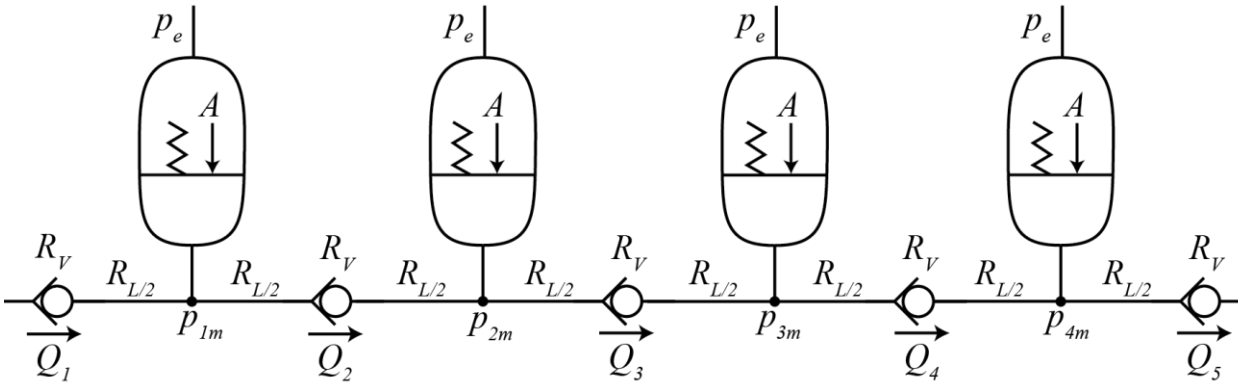

Figure 2.1. Hydraulic schematic of a lymphatic system with four lymphangions connected in series.

The flow rate (Q_i) is a function of the valve resistance (R_{vi}) that varied with applied pressure difference across the valve (Δp_{vi}) based on the following relationship-

$$Q_i = \frac{\Delta p_{vi}}{R_{vi}} \tag{2}$$

The valve resistance (R_{vi}) can be obtained by the following equation-

$$R_{vi} = R_{vn} + R_{vx}\left[\frac{1}{1+\exp\left(s_{open}\left(\Delta p_{vi} - p_{open}\right)\right)} + \frac{1}{1+\exp\left(-s_{fail}\left(\Delta p - p_{fail}\right)\right)} - 1\right] \quad (3)$$

Here, R_{vn} and R_{vx} are the minimum and maximum valve resistances determined by valve opening slope (s_{open}), valve opening pressure (p_{open}), valve failure slope (s_{fail}), and valve failure pressure (p_{fail}).

Each vessel segment can be further described by the following relationship based on the conservation of fluid mass-

$$\frac{dD_i}{dt} = \frac{2}{\pi D_i L}\left(Q_i - Q_{i+1}\right) \quad (4)$$

Here, $\frac{dD_i}{dt}$ is the change in vessel diameter over time (t) and L is the lymphangion length. The flow inside the lymphatic vessels had a fluid viscosity (μ) that characterized the linear flow resistance (R_L), given by the following equation-

$$R_L = \frac{64\mu L}{\pi {D_i}^4} \quad (5)$$

A vessel wall constitutive relation including passive and periodic contractile components was used to obtain the following time-varying relationship between the transmural pressure (p_{tm}), maximum active tension (M), contraction frequency (f), and vessel diameter (D_i)-

$$p_{tm} = \Phi(D_i;\ P_{di}, D_{di}) + A(t, D_i; M, f, t_{0i}) \quad (6a)$$

$$\Phi(D_i; P_{di}, D_{di}) = P_{di}\left(e^{\frac{D_i}{D_{di}}} - \left(\frac{D_{di}}{D_i}\right)^3\right) \quad (6b)$$

$$A(t, D_i; M, f, t_{0i}) = \frac{M}{D_i}\left(1 - \cos\left(2\pi f(t - t_{0i})\right)\right) \quad (6c)$$

Here, Φ is the constitutive relation for the nonlinear fluid capacitance representing the stretch of the lymphangion wall and A is the active tension. P_{di} and D_{di} are constitutive relation parameter

values, and t_{0i} is the start time of the active tension which sets the phase of the lymphangion contraction relative to the other lymphangions in the network.

For each lymphangion valve, the above equations were solved computationally by using MATLAB Simulink ode23tb to obtain the flow rate (Q_i) as a function of time. For simplicity, the following valve and non-valve parameters were chosen to be constant for all four lymphangions, Table 2.1.

Table 2.1. Parameter values used for simulation of four-vessel lymphangion network system.

Definition	Denote	Value	Unit (CGS)
Valve failure pressure	p_{fail}	-1.8×10^4	$\mathrm{dyn.\,cm^{-2}}$
Valve failure slope	s_{fail}	4.9×10^{-2}	$\mathrm{cm^2.\,dyn^{-1}}$
Maximum valve resistance	R_{vx}	1.2×10^7	$\frac{\mathrm{dyn.\,cm^{-2}}}{\mathrm{cm^3.\,s^{-1}}}$
Minimum valve resistance	R_{vn}	600	$\frac{\mathrm{dyn.\,cm^{-2}}}{\mathrm{cm^3.\,s^{-1}}}$
Valve opening slope	s_{open}	0.04	$\mathrm{cm^2.\,dyn^{-1}}$
Valve opening pressure	p_{open}	-70	$\mathrm{dyn.\,cm^{-2}}$
Fluid viscosity	μ	0.01	$\frac{\mathrm{dyn.\,s}}{\mathrm{cm^2}}$
Lymphangion length	L	0.3	cm
Constitutive-relation constant (pressure)	P_{di}	50	$\mathrm{dyn.\,cm^{-2}}$
Constitutive-relation constant (diameter)	D_{di}	0.025	cm
Contraction frequency	f	0.5	Hz
Inlet pressure	p_a	2275	$\mathrm{dyn.\,cm^{-2}}$
Outlet pressure	p_b	2375	$\mathrm{dyn.\,cm^{-2}}$

With other parameters like the lymphangion length (L) and the inlet and outlet pressure (p_a and p_b) kept constant, the flow rate (Q_i) depends on the maximum active tension (M) that declines in the case of damaged lymph nodes, resulting a lower flow rate [32]. Hence, the simulation included the following scenarios-

- A constant external pressure ($p_{ei} = 2100\ \text{dyn.cm}^{-2}$) with maximum active tension ($M = 3.6\ \text{dyn.cm}^{-1}$) that indicated an undamaged lymphatic system.
- A constant external pressure ($p_{ei} = 2100\ \text{dyn.cm}^{-2}$) with lower values of maximum active tension $M = \{3.0, 2.5, 2.0, 0.5\}\ \text{dyn.cm}^{-1}$ that indicated a damaged lymphatic system.
- A variable external pressure with the lowest value of the maximum active tension ($M = 0.5\ \text{dyn.cm}^{-1}$) that indicated the application of pneumatic compression treatment for a damaged lymphatic system. The sequence for the application of variable external pressure is given by Figure 2.2.

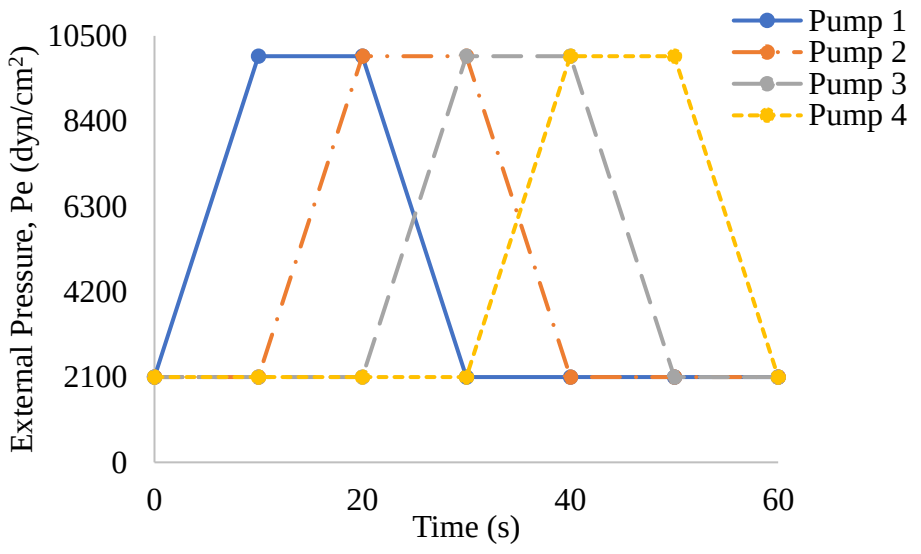

Figure 2.2. Sequence for application of variable external pressure to vessel segments.

The pumps operated between the initial external pressure of 2100 $\mathrm{dyn.\,cm^{-2}}$ and a higher external pressure of 10000 $\mathrm{dyn.\,cm^{-2}}$. The external pressure sequence simulated a typical compression technique applied by pneumatic pumps for upper extremity lymphedema [20].

2.2. Design of Compression Subsystem

2.2.1. Compression Garment

The compression garment used for treating upper extremity lymphedema can have multiple chambers. The number of chambers typically ranges from 3 to 12; however, there is no uniform criteria for selection of this parameter [33]. In this study, a compression garment consisting of four separate chambers was made, as depicted in Figure 2.3.

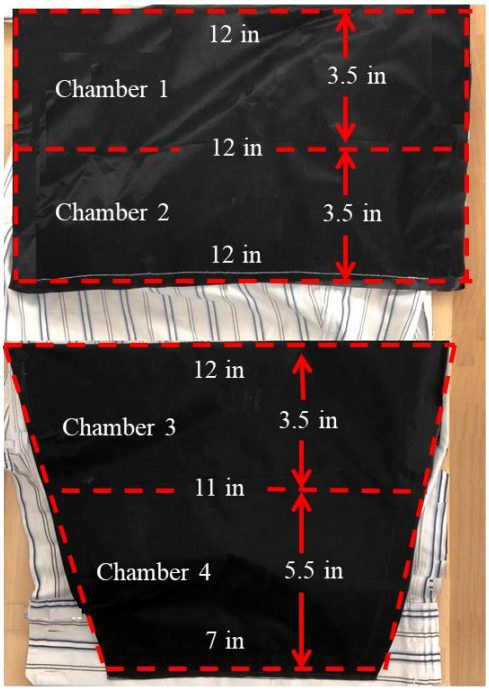

Figure 2.3. Chamber specifications of prototype compression sleeve.

The chambers were cut from a single sheet of heat sealable, polymer-coated nylon fabric (Seattle Fabric Inc., Seattle, Washington, USA) and sealed using an impulse sealer. The fabric was chosen for its anti-microbial and fire retardant properties, and high thermal and chemical stability [34]. Adjustable straps (VELCRO, Manchester, New Hampshire, USA) were sewn onto the outside so the sleeve could be easily attached and removed.

2.2.2. Pneumatic Pumps

Four 22K series 4.5 V DC-motor-driven gas diaphragm pumps manufactured by Boxer GmbH (Ottobeuren, Germany) were used for applying compression to the chambers. Each pump was rated for a maximum pressure of 300 mbar (225 mmHg). The outlet valves of the pumps were connected to the compression garment chambers by a silicone rubber tube with an outer diameter of 6.50 mm and an inner diameter of 3.50 mm. The silicone rubber tube was glued to each of the four chambers that enabled the chambers to inflate and deflate separately, Figure 2.4.

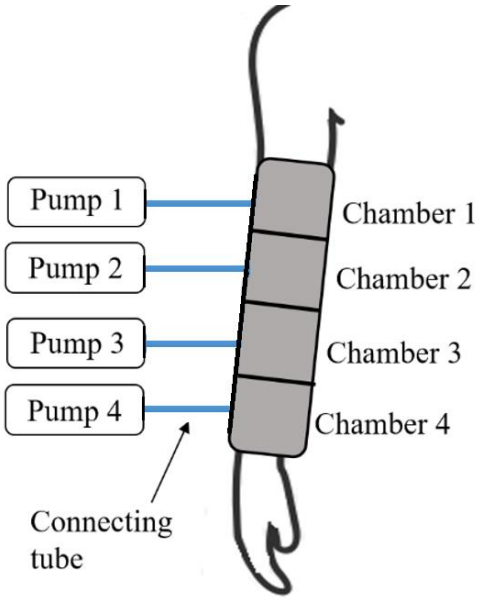

Figure 2.4. Schematic of four compression chambers connected to pneumatic pumps.

2.2.3. Sequential Operation of Pumps

A compression circuit system was built for a sequential maneuver of the pumps for a total duration of 180 seconds that indicated one full compression cycle, Figure 2.5. The compression cycle was divided into four phases. Phase 1 denoted the operation of Pump 1 from 0 to 30 seconds. Phase 2 denoted the operation of Pump 1 and Pump 2 from 30 to 60 seconds. Phase 3 denoted the operation of the first three pumps from 60 to 90 seconds and Phase 4 denoted the operation of all four pumps from 90 to 180 seconds.

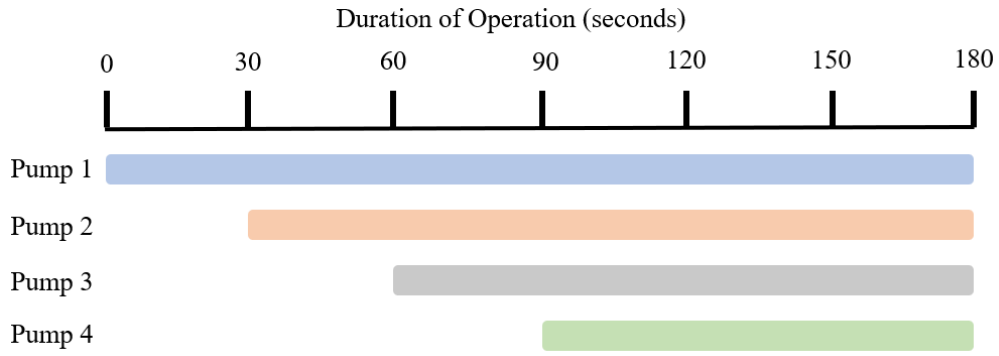

Figure 2.5. Sequential operation of pumps for a total duration of 180 seconds.

The sequential operation inflated the chambers one by one from proximal (upper arm) to distal (lower arm) with the maximum pressure in a chamber not to exceed 60 mmHg [35]. With this setup, a time versus pressure curve was obtained as each chamber reached a pressure of 10, 20, 30, 40, and 50 mmHg. A voltage versus pressure curve was also obtained for the chambers.

2.3. Design of BIA Subsystem

Performing a BIA analysis typically includes a hand-to-hand mode or a foot-to-foot mode in which the path of current flows through respective limbs [36]. The procedure involves attaching a number of contact electrodes to measure body impedance values. By combining hand

and foot contact plates with a fixed measuring circuit, a multi-segmental impedance measurement system can also be developed for a BIA analysis.

2.3.1. Development of Test Circuit

A test circuit equivalent to the human arm model was developed as a part of designing the BIA subsystem, Figure 2.6 [37]. Resistors R1 and R4 modeled the resistance of the electrode-skin interface. Resistors R2 and R3 modeled the intra-cellular fluid (ICF) and extra-cellular fluid (ECF) respectively (see Figure 1.5) and are mentioned as the 'test circuit impedance' throughout this study. The cell membrane capacitor C1 was in series with ICF resistor R2 and parallel with ECF resistor R3.

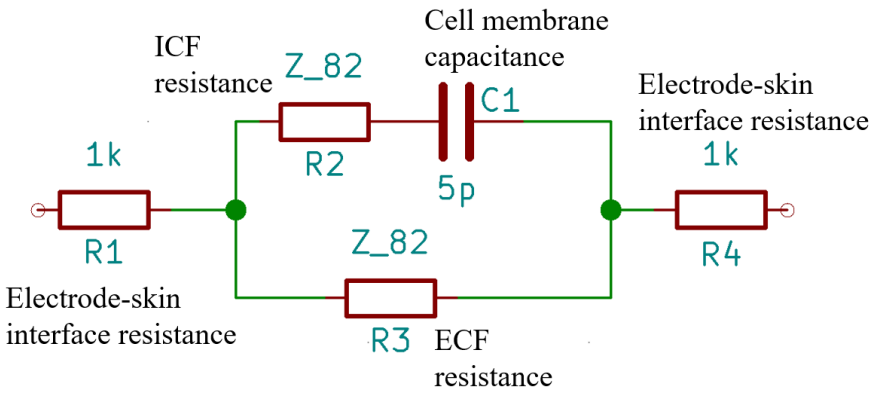

Figure 2.6. Schematic of test circuit used in BIA subsystem.

The test circuit impedance is a frequency-dependent variable impedance with a resistive (real) part and a reactive (imaginary) part. At very low frequency, the cell membranes act as an effective barrier to AC current that makes the current to pass around the cell membranes (refer to Figure 1.5). For a very high frequency, the current passes directly through the cell membrane and no capacitance is observed. At medium range frequencies, the cell membranes act as capacitors and the phase differences between the current intensity and voltage drop are observed. In

practice, the phase difference for biological tissues are typically below 10 degrees or 0.17 rad [38].

For the BIA subsystem, an initial test circuit included an ECF and ICF impedance of 82 Ω (denoted by Z_{82}). Measured at zero frequency with a calibrated LCR meter (B&K Precision Model 894, Yorba Linda, California, USA) [39], the actual DC resistance for Z_{82} was 81.81 Ω. Measured in the limit as frequency increases, the test circuit impedance theoretically decreases to a limiting value of 41 Ω. Practically, parasitic effects mean that at extremely high frequencies, inductive effects take over, increasing the total impedance. The change in impedance with varying frequency was measured with the LCR meter.

2.3.2. Relationship between ECF Volume and ECF Resistance

The relationship between ECF volume (V_{ECF}) and ECF resistance (or in this case, test circuit impedance) (Z) can be given by the following equation [38], [40]-

$$V_{ECF} = k_{ECF}\left(\frac{H^2\sqrt{W}}{Z}\right)^{2/3} \tag{7}$$

where H and W are the height and weight of the individual expressed in cm and kg respectively. The factor k_{ECF} depends on ECF resistivity (ρ_{ECF}) expressed in Ω-cm, and body density (D_b) expressed in $\frac{g}{cm^3}$. The value of k_{ECF} can be further calculated by the following equation-

$$k_{ECF} = \frac{1}{100}\left(\frac{{K_B}^2{\rho_{ECF}}^2}{D_b}\right)^{1/3} \tag{8}$$

where K_B is a factor based on approximation of individual geometry. For measurements of V_{ECF}, k_{ECF} can be approximated as 0.306 for men and 0.316 for women [40]. A 3% change in V_{ECF} can be an indication of lymphedema related swelling [41].

2.3.3. Development of BIA Circuit

A BIA circuit was built to provide single and multi frequency impedance measurements of the test circuit, Figure 2.7. The circuit performance was simulated using TINA-TI analog electronic circuit simulator.

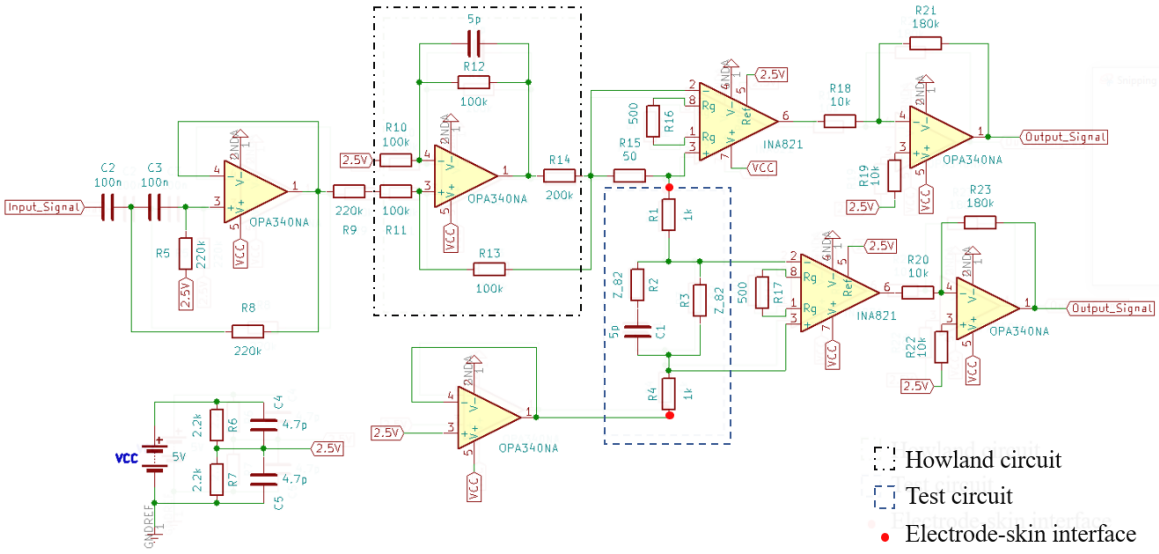

Figure 2.7. Schematic of BIA circuit developed for impedance measurements of a test circuit.

A virtual ground circuit was used to create a mid-supply rail, consisting of a resistor divider and op-amp follower (OPA 340, Texas Instruments) in a unity gain configuration. Thus, for the signal conditioning circuitry, the power supply system consisted of a high-side supply of +2.5 V and a low-side supply of -2.5 with the virtual ground in between. The 5 V power input was provided by a Zeee 5200 mAh 7.4 V battery (Zeee Power, Houizhou, Guangdong, China).

An OPA 340 op-amp was used as the basis of a Howland current source circuit in the BIA subsystem. The positive and negative feedback paths of the Howland circuit were balanced through a matched resistor array consisting of four resistors (R11 to R13) of 100 kΩ (ORNTA1003AT1, Vishay Intertechnology) with a precision of ±0.1%. As a result, a voltage-

controlled current source was obtained [42]. A resistor of 500 Ω was placed across the R_g pins (R16 and R17) of the in-amps to achieve a differential gain of G = 99.8, [43]. This gain value was used to achieve a high common-mode rejection ratio (CMRR) which can be represented by the following equation-

$$\mathrm{CMRR} = \left(\frac{A_d}{|A_{CM}|}\right) = 10\log_{10}\left(\frac{A_d}{|A_{CM}|}\right)^2 \mathrm{dB} = 20\log_{10}\left(\frac{A_d}{|A_{CM}|}\right)\mathrm{dB} \quad (9)$$

Here, A_d is the differential gain (G) and A_{CM} is the common-mode gain. Hence, a high value for A_d ensured the amplification of required differential signals while rejecting unwanted common-mode signals. A final gain stage was implemented with an inverting amplifier (OPA 340) with a gain of 18 [44]. Two instrumentation amplifiers (INA 821, Texas Instruments) measured the output voltage drops across both the test circuit impedance (Z_{82}) and a known reference impedance (R15) of $50\ \Omega$ placed in series with the test circuit impedance.

The maximum voltage that could be supplied to the circuit was limited by the 7.4 V voltage of the battery. The use of a 200 kΩ resistor (R14) reduced the possibility of a large current development in the test circuit. Moreover, a very low probabilty of short-cricuit failure mode for film type resistors [45] enhanced the safety features of the circuit.

2.3.4. BIA Subsystem for Single Frequency Impedance Measurement

2.3.4.1. Configuration of Microcontroller as Signal Generator

An Arduino UNO Rev3 microcontroller board based on an 8-bit ATmega328P-PU microcontroller was used to generate a pulse-width modulation (PWM) signal for the BIA circuit in a 'Phase and Frequency Correct' mode [46], [47], Figure 2.8. The PWM signal frequency (f_{PWM}) was calculated by using the following equation-

$$f_{PWM} = \frac{f_{CLK}}{2 \times N_p \times TOP} \quad (10)$$

Here, f_{CLK} is the 16 MHz clock frequency of the microcontroller, N_p is the prescaler divider value and TOP is the timer/counter top set in the Input Capture Register 1 (ICR1) of the microcontroller. With the 16-bit timer, the highest TOP value of 0xFFFF or 65536 was obtained from ICR1. For a presecaler divider (N_p) value of 1, a 122.07 Hz PWM frequency (f_{PWM}) was obtained.

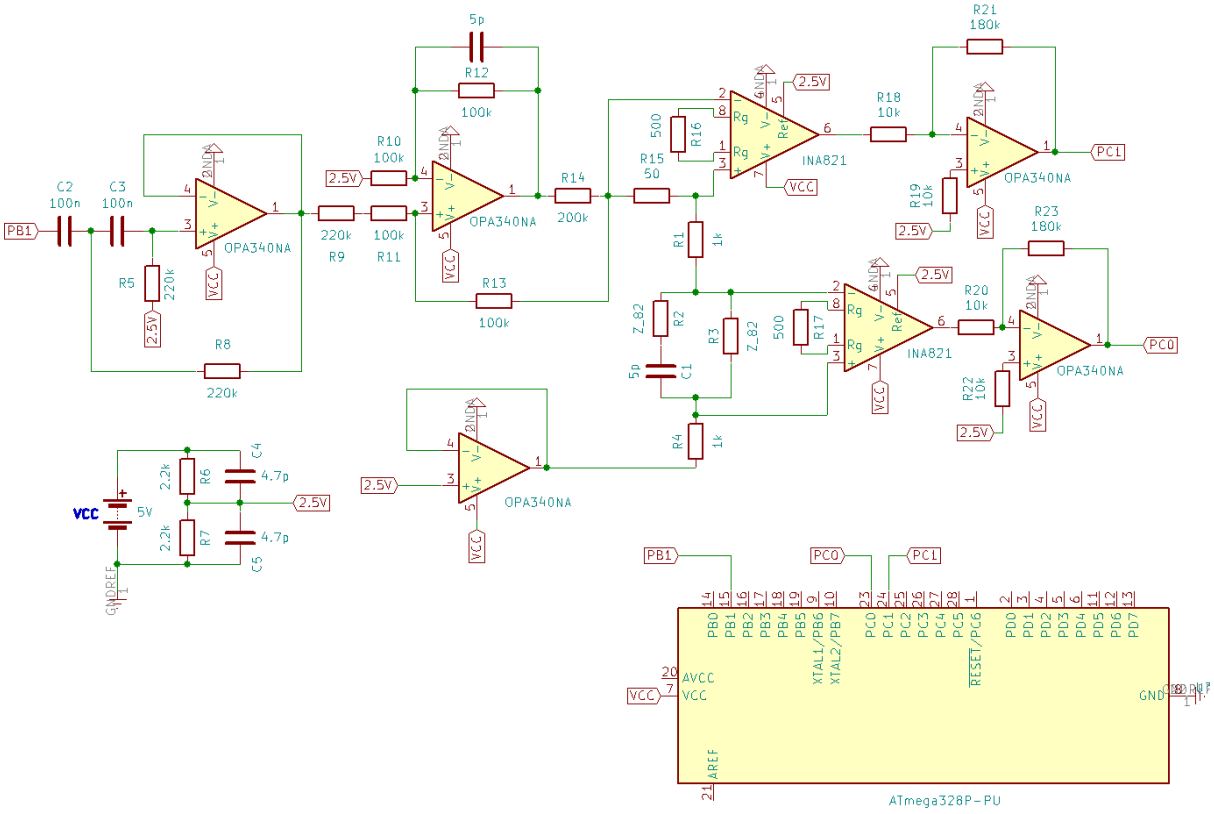

Figure 2.8. Use of ATmega328P-PU as signal generator for BIA circuit.

The hexadecimal representation of the final fuse configuration for the microcontroller is given by the following-

Low- 0xBF

High – 0xDE

Extended- 0x05

The internal 10-bit analog-to-digital converter (ADC) of the microcontroller was used to convert the analog signal into a digital signal.

The analog input pin PC0 of the microcontroller recorded the voltage drop across the test circuit impedance whereas the analog input pin PC1 recorded the voltage drop across the reference impedance.

2.3.4.2. Calculating Fourier Coefficients of Signal Frequency

The Fourier coefficient for a measured signal $x(t)$ sampled at times $i\Delta t$, $(i = 1, \dots, N)$ can be approximated by the following rectangular-windowed discrete transform-

$$c_N = \frac{2}{N}\sum_{i=1}^{N}(\cos(2\pi f_b i\Delta t) + i\sin(2\pi f_b i\Delta t))x(i\Delta t) \tag{11}$$

In the above equation, the number of samples N was selected as

$$N \in \{100, 200, 500, 1000, 2000, 5000\}$$

for the calculation of Fourier coefficient. The number of samples is a tradeoff between the time to finish the measurement and the accuracy. Considering a partial sum to find a recursive algorithm for computation of c_N, the Fourier coefficient was calculated as-

$$c_j = \frac{2}{j}\left(\frac{j-1}{2}c_{j-1} + (\cos(2\pi f_b j\Delta t) + i\sin(2\pi f_b j\Delta t))x(j\Delta t)\right) \tag{12}$$

$$= \frac{j-1}{j}c_{j-1} + \frac{2}{j}(\cos(2\pi f_b j\Delta t) + i\sin(2\pi f_b j\Delta t))x(j\Delta t)$$

The Coordinate Rotation Digital Computer (CORDIC) algorithm was used to calculate trigonometric functions in the above Fourier coefficients formula [48]. With the time sampling interval (Δt) set at 25 μs, the algorithm was formulated to calculate the Fourier coefficient of the

PWM signal frequency of 122.07 Hz and a sampling frequency of 500 Hz. A total of 20 measurements were obtained for each number of samples (N).

A fixed-point arithmetic was used for the ATmega328P-PU microcontroller to perform required computations and ensure that calculations can be performed at the required sample rates [47]. A fixed-point arithmetic library, AVRfix was used for all fixed-point calculations. Based on the ISO/IEC 18037 standard, the signed _Accum s15.16 bit fixed-point data type was used for calculations[49].

2.3.4.3. Calculations of Ratio of Amplitudes and Phase Difference between Output Signals

The output of the discreet Fourier transform algorithm consists of a real part (Re) and an imaginary part (Im). The ratio of amplitude of the output signals (γ) was calculated by using the following equations-

$$\text{Amplitude of output signal obtained from analog input pin PC0 } (\gamma_1) = \sqrt{(\text{Re})_1{}^2 + (\text{Im})_1{}^2}$$

$$\text{Amplitude of output signal obtained from analog input pin PC1 } (\gamma_2) = \sqrt{(\text{Re})_2{}^2 + (\text{Im})_2{}^2}$$

$$\text{Ratio of amplitude } (\gamma) = \frac{\gamma_1}{\gamma_2}$$

The phase difference (Φ) between the two output signals was also obtained by using the following equations-

$$\text{Phase of output signal obtained from analog input pin PC0 } (\Phi_1) = \text{atan } (\frac{\text{Im}_1}{\text{Re}_1})$$

$$\text{Phase of output signal obtained from analog input pin PC1 } (\Phi_2) = \text{atan } (\frac{\text{Im}_2}{\text{Re}_2})$$

$$\text{Phase difference } (\Phi) = |\Phi_1 - \Phi_2|$$

Using the above equations, the mean values of ratio of amplitudes (γ) and phase difference (Φ) were obtained for the specified number of samples (N). The accuracy of measurements was estimated based on a 95% confidence interval for the 20 data points.

2.3.4.4. Comparison between Test Circuit Impedance and Measured Impedance

The ratio of output signal amplitudes (γ) was multiplied by the reference impedance (50 Ω) to measure the impedance of the body (or, in this case, a phantom test circuit). To compare the measured impedance with the test circuit impedance, the following set of nine variable test circuit impedance (measured by a high accuracy LCR meter at zero frequency) were considered for the BIA subsystem along with the initial impedance of Z_{82}-

Denote	Z_{74}	Z_{76}	Z_{78}	Z_{80}	Z_{82}	Z_{84}	Z_{86}	Z_{88}	Z_{90}
Z (Ω)	74.05	75.95	77.78	80.22	81.81	83.56	86.06	88.21	90.34

For each of the nine test circuit impedances, the standard value of ratio of amplitude (γ) was calculated based on the 50 Ω reference impedance. A percentage of error between the test circuit impedance and the measured impedance was obtained for specified number of samples (N). The percentage of error was averaged over N to get the error range for all nine test circuit impedance values.

2.3.4.5. Sensitivity Analysis of Measured Impedance

The percentage of error between the test circuit impedance and the measured impedance was used to analyze the sensitivity of the BIA circuit. For an average percentage of error in measured impedance, the corresponding error in ECF volume was calculated based on equations (7) and (8). The range of error was then used to determine the sensitivity of the BIA circuit that could be used for detection of swelling.

2.3.5. BIA Subsystem for Multi frequency Impedance Measurement

2.3.5.1. Multiple Frequency Testing

A Mixed Signal Oscilloscope (Keysight InfiniiVision MSOX3024T) was used to capture the output signals from the two instrumentation amplifiers, Figure 2.9. The oscilloscope's built-in waveform generator was set to generate square waves of frequencies

$$f = \{100, 500, 1k, 5k, 10k, 20k, 40k, 60k, 80k, 100k\}\ Hz$$

across the inputs to the Howland circuit.

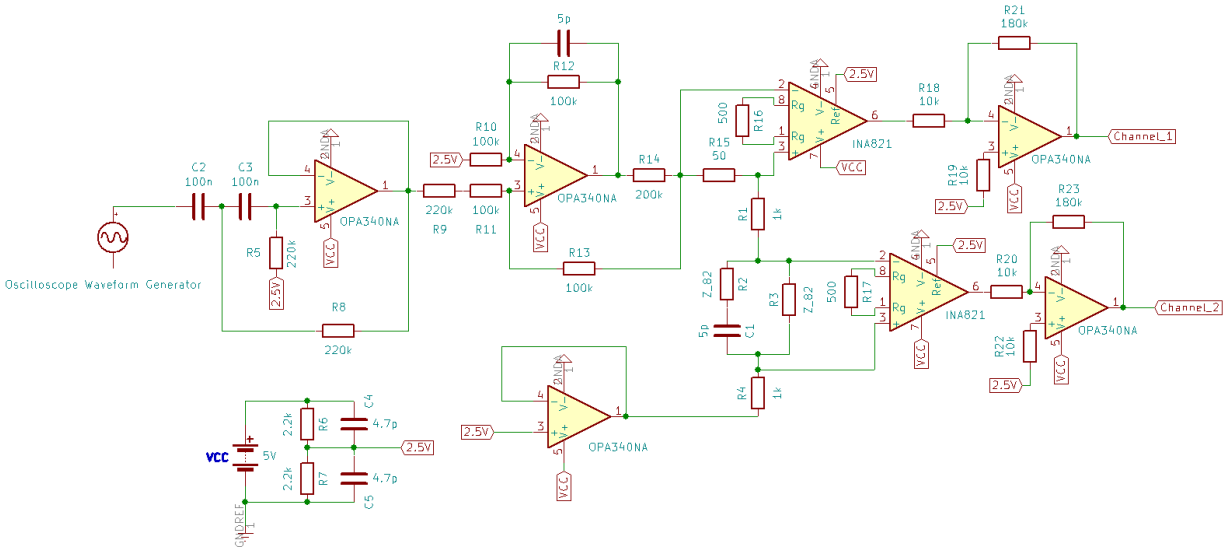

Figure 2.9. Use of oscilloscope as signal generator for BIA circuit.

Channel 1 of the oscilloscope measured the voltage drop across the reference impedance (50 Ω) whereas Channel 2 measured the voltage drop across the test circuit impedance (Z_{74} to Z_{90}).

2.3.5.2. Generation of Nyquist Plot

The waveform data obtained from oscilloscope was imported to MATLAB and the Fourier coefficients of the periodic voltage measurements of the test circuit resistance at

frequency f_i, labeled R_i, and the test circuit reactance at frequency f_i, labeled X_i, were calculated at each of the test frequencies to generate the Nyquist plot. The MATLAB trapezoidal numerical integration method was used to calculate the Fourier coefficients for signals obtained from Channel 1 and Channel 2 of the oscilloscope with a sampling time $dt = 8 \times 10^{-10}$ seconds. The following equations describe the calculation, where τ is the signal period.

$$A_i = \int_0^{N\tau} e^{j\omega_i t} V_{ref}(t)\, dt \tag{13a}$$

$$B_i = \int_0^{N\tau} e^{j\omega_i t} V_{test}(t)\, dt \tag{13b}$$

$$\omega_i = 2\pi f_i \tag{13c}$$

$$R_i + jX_i = \frac{B_i}{A_i} R_{ref} \tag{13d}$$

The Nyquist plot was validated by using the calibrated LCR meter that measured the resistance and reactance of the test circuit at the same signal frequencies with 4-wire Kelvin clips. A comparison was made between the prototype BIA measurements and LCR meter measurements of test circuit impedance at room temperature (72 F) over the specified frequency range. The comparison was based on the 'Magnitude Ratio' that can be calculated by the following equation-

$$\text{Magnitude ratio (m)} = \frac{\text{Test circuit impedance magnitude obtained from prototype}}{\text{Test circuit impedance magnitude measured by LCR meter}}$$

2.3.5.3. Temperature Stability

The temperature stability of the BIA circuit was examined to observe changes in the Nyquist plot for test circuit impedance Z_{74} at temperatures higher than the room temperature (72 F) to simulate potential variability in the environment of the measurement device. A hot plate was used to slowly heat the BIA circuit until the temperature reached the target values of $T = \{75, 80, 85, 90\}$ F. Once the target temperature was reached, the oscilloscope was used to obtain waveform data. Voltage drops across the reference impedance and the test circuit impedance were captured to generate Nyquist plots similar to the previously described method.

2.4. Calculation of Battery Life and Number of Compression Cycles

Both the compression subsystem and the BIA subsystem were powered by a Zeee 5200 mAh 7.4 V battery. For the compression subsystem, the four phases $(p = 1, 2, 3, 4)$ contributed to the average current draw over one compression cycle of 180 seconds. An ammeter was used to measure the average current draw at each of the four phases. The weighted average for compression subsystem ($I_{avg-compression}$) was calculated by the following equation-

$$I_{avg-compression} = \frac{\sum_{p=1}^{4} I_p \times T_p}{180} \tag{14}$$

where I_p is the average current draw by phase p and T_p is the duration of phase p.

For the BIA subsystem, the Arduino board ($I_{avg-arduino}$), microcontroller ($I_{avg-microcontroller}$), and Howland circuit ($I_{avg-Howland}$) contributed to the average current draw ($I_{avg-BIA}$) over one compression cycle of 180 seconds. The weighted average was calculated by the following equation-

$$I_{avg-BIA} = I_{avg-arduino} + I_{avg-microcontroller} + I_{avg-Howland} \tag{15}$$

The average power draw by the compression subsystem and the BIA subsystem was calculated based on the average current draw over one compression cycle by those subsystems and the supply voltage. The battery life was calculated based on the battery capacity and the total average power draw over one compression cycle by the subsystems. The estimated total number of compression cycles was calculated based on the battery life and the duration of each compression cycle.

CHAPTER 3. RESULTS AND ANALYSIS

3.1. LYMPHATIC SYSTEM

Figure 3.1 shows the flow rates (Q_i) obtained from five valves ($i = 1, 2, 3, 4, 5$) for a maximum active tension $M = 3.6$ dyn. cm^{-1} and a constant external pressure $p_e = 2100$ dyn. cm^{-2}, indicating an undamaged lymphatic system. The value of the maximum flow rate ranged between 1.36 cc/hr for Q_1 and 0.65 cc/hr for Q_5.

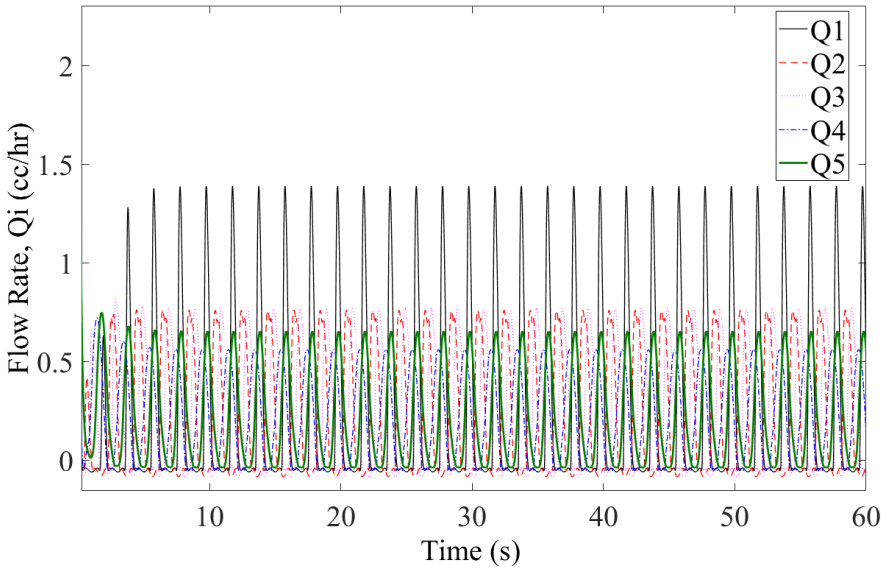

Figure 3.1. Flow rates obtained from different valves of lymphangion chain network for a maximum active tension $M = 3.6$ dyn. cm^{-1} and a constant external pressure $p_e = 2100$ dyn. cm^{-2}.

Figure 3.2 shows the changes in flow rate Q_5 observed in the last valve ($i = 5$) of the lymphangion chain network for different values of maximum active tension (M). As the tension decreased from $M = 3.6$ dyn. cm^{-1} to $M = 0.5$ dyn. cm^{-1} (indicating damage to the lymphatic system), the flow rate reduced from 0.65 cc/hr to 0.05 cc/hr.

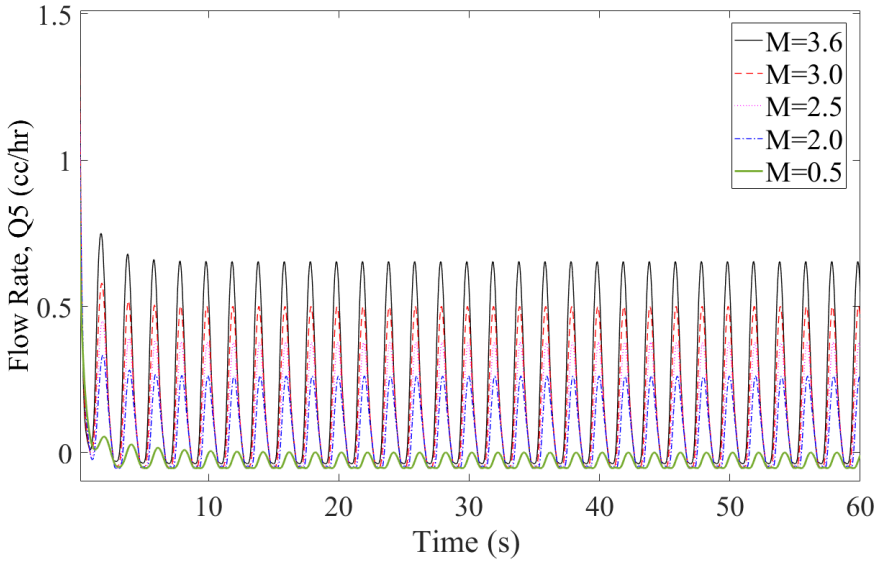

Figure 3.2. Changes in flow rate observed in the last valve ($i = 5$) of the lymphangion chain network as the maximum active tension (M) reduced from 3.6 dyn. cm^{-1} to 0.5 dyn. cm^{-1}.

Figure 3.3 shows the flow rate Q_5 observed for the lowest value of the maximum active tension ($M = 0.5$ dyn. cm^{-1}) under the application of an additional variable external pressure (see Figure 2.2) that indicated a typical pneumatic compression treatment sequence. The data was compared to the flow rate obtained for a constant external pressure $p_e = 2100$ dyn. cm^{-2}. An average of 19% increase in flow rate was observed in the case of the additional variable external pressure.

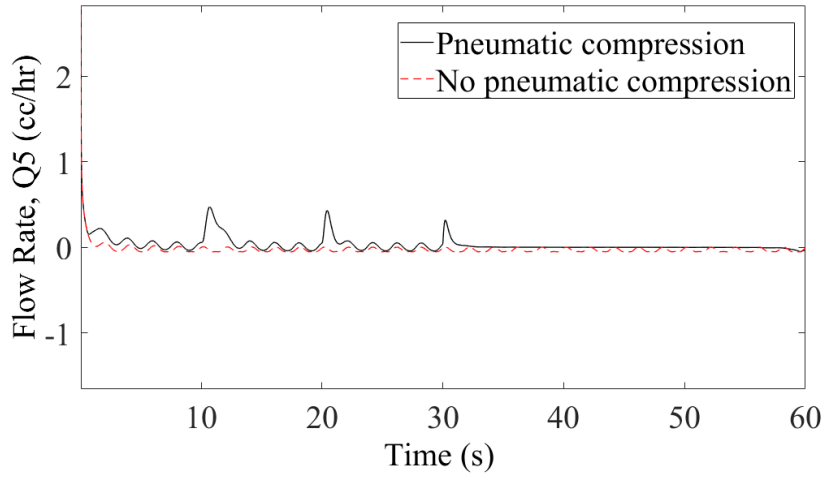

Figure 3.3. Comparison of flow rate (Q_5) between an additional variable external pressure (pneumatic compression) and a constant external pressure (no pneumatic compression) for the lowest value of maximum active tension.

3.2. COMPRESSION SUBSYSTEM

Table 3.1 shows the maximum pressure measured at each compression chamber for one full compression cycle of 180 seconds. The maximum pressure in the chambers ranged between 53.1 mmHg and 54.0 mmHg. It was observed that once reached, the maximum pressure was maintained by all four chambers throughout the duration of operation.

Table 3.1. Maximum pressure measured at each compression chamber for a compression cycle of 180 seconds.

	Maximum Pressure (mmHg)
Chamber 1	53.1
Chamber 2	53.1
Chamber 3	54.0
Chamber 4	53.6

Figure 3.4 shows the time required for individual chambers to reach 10, 20, 30, 40, and 50 mmHg of pressure. The average time required for the chambers to reach 50 mmHg pressure was 75 seconds.

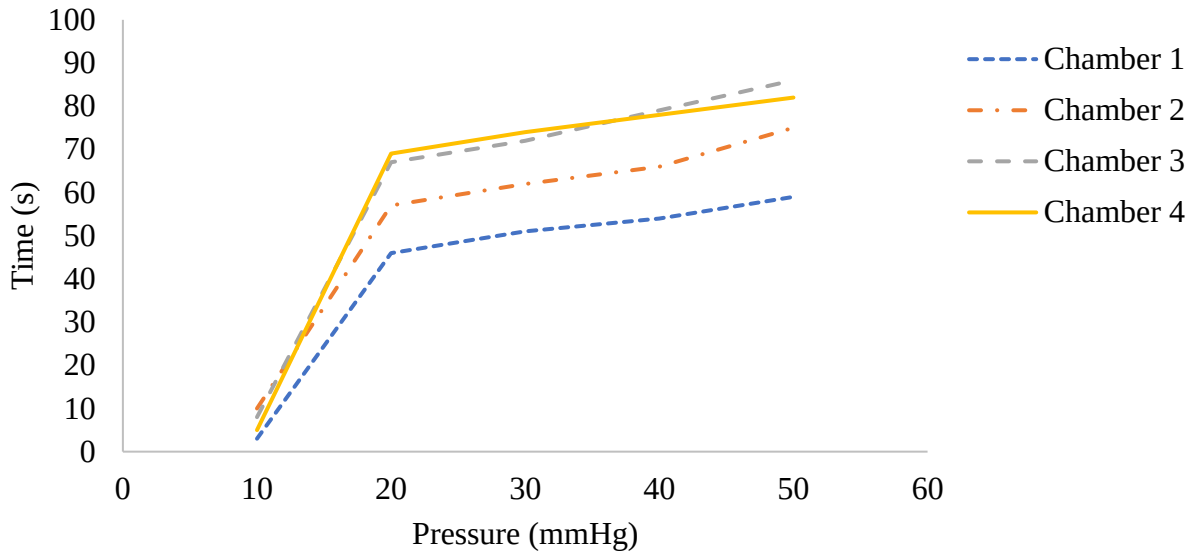

Figure 3.4. Time required for four pneumatic compression chambers to reach target pressure.

Figure 3.5 shows the voltage vs pressure curve for the chambers. The highest pressure of 117 mmHg was observed in Chamber 1 for a 6 V supply whereas the lowest pressure of 6 mmHg was observed in Chamber 3 for a 4 V supply. All four chambers had a pressure range of 50 mmHg to 60 mmHg for a supply of 5 V.

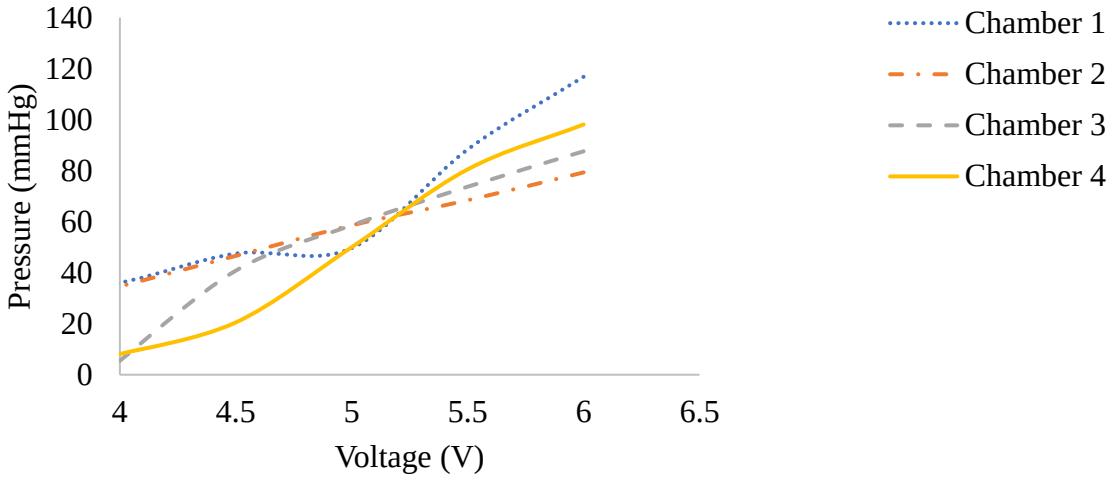

Figure 3.5. Voltage vs pressure curve for four pneumatic compression chambers. The supply voltage ranged from 4 V to 6 V.

3.3. BIA SUBSYSTEM

3.3.1. Single Frequency Impedance Measurement

Figure 3.6 to Figure 3.14 show the mean values of ratio of amplitudes (γ) and phase difference (Φ) between two output signals. The measurements were taken at number of samples $N \in \{100, 200, 500, 1000, 2000, 5000\}$ for variable test circuit impedance Z_{74} to Z_{90}. The standard value of γ calculated from the reference impedance (50 Ω) and test circuit impedance is also shown in the figures.

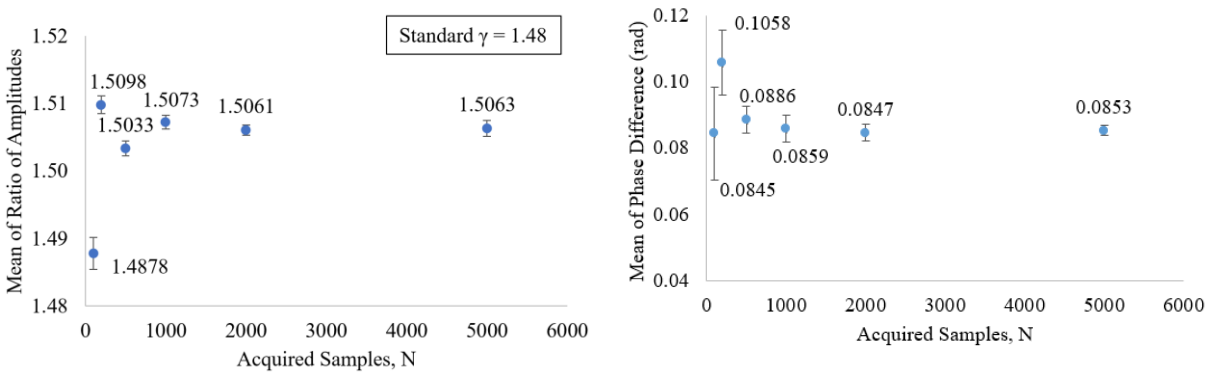

Figure 3.6. Mean of ratio of amplitudes and phase difference for Z_{74}.

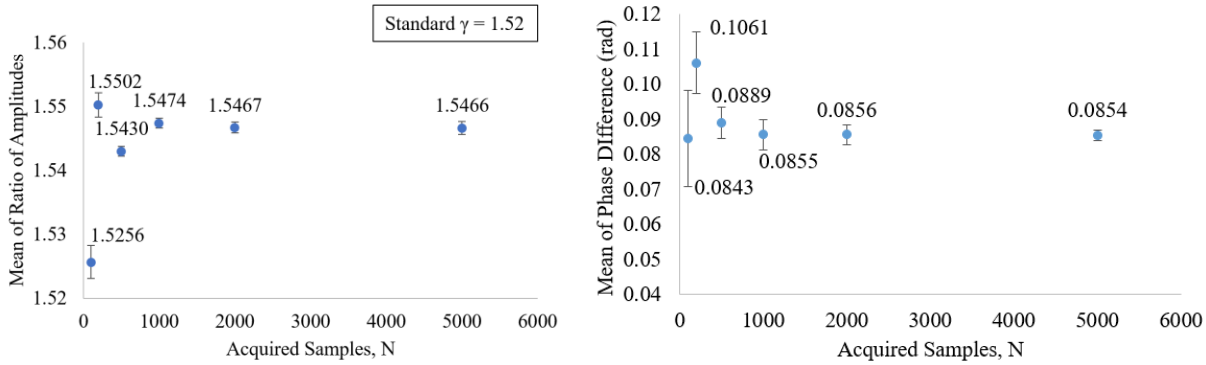

Figure 3.7. Mean of ratio of amplitudes and phase difference for Z_{76}.

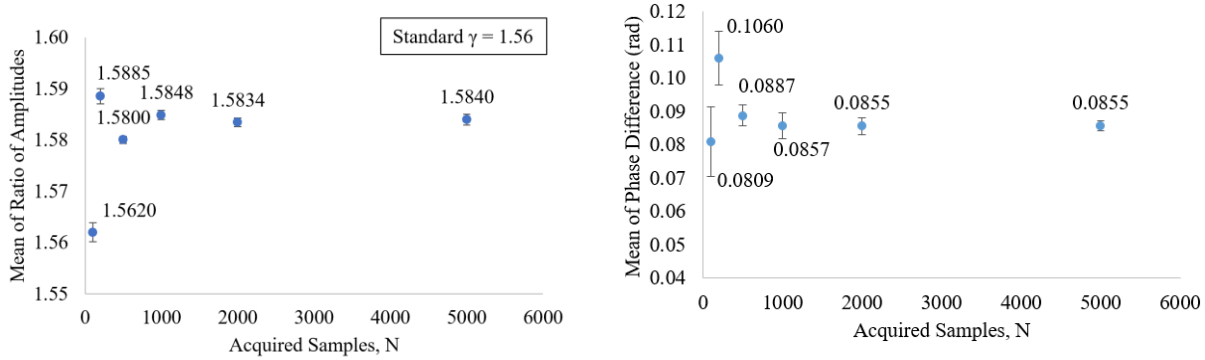

Figure 3.8. Mean of ratio of amplitudes and phase difference for Z_{78}.

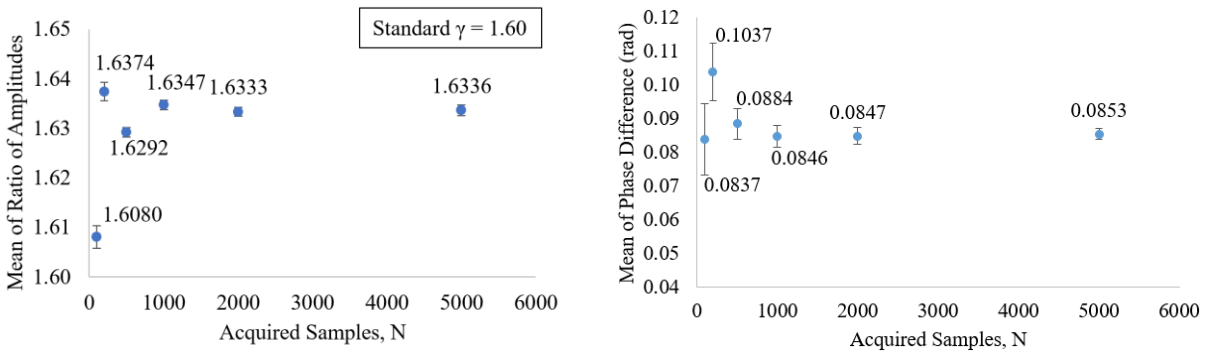

Figure 3.9. Mean of ratio of amplitudes and phase difference for Z_{80}.

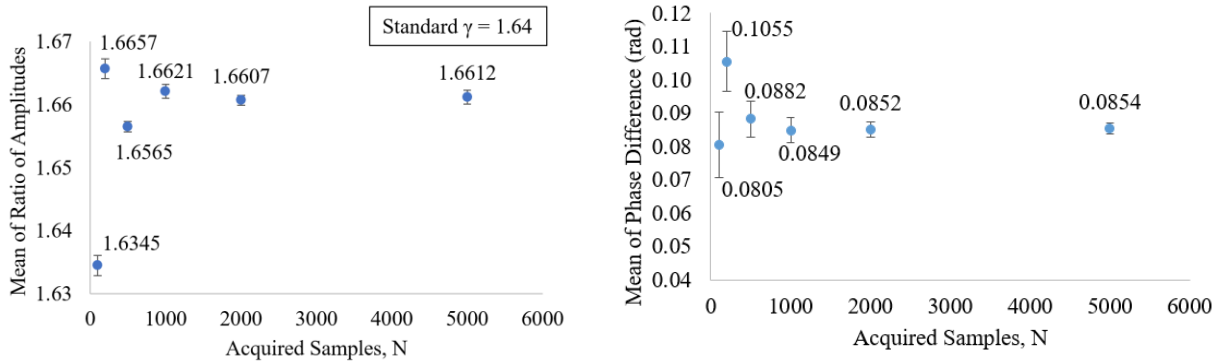

Figure 3.10. Mean of ratio of amplitudes and phase difference for Z_{82}.

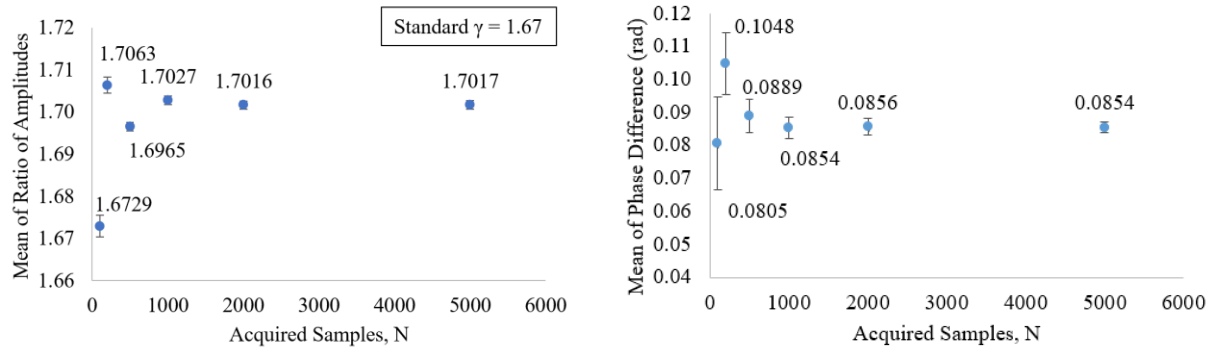

Figure 3.11. Mean of ratio of amplitudes and phase difference for Z_{84}.

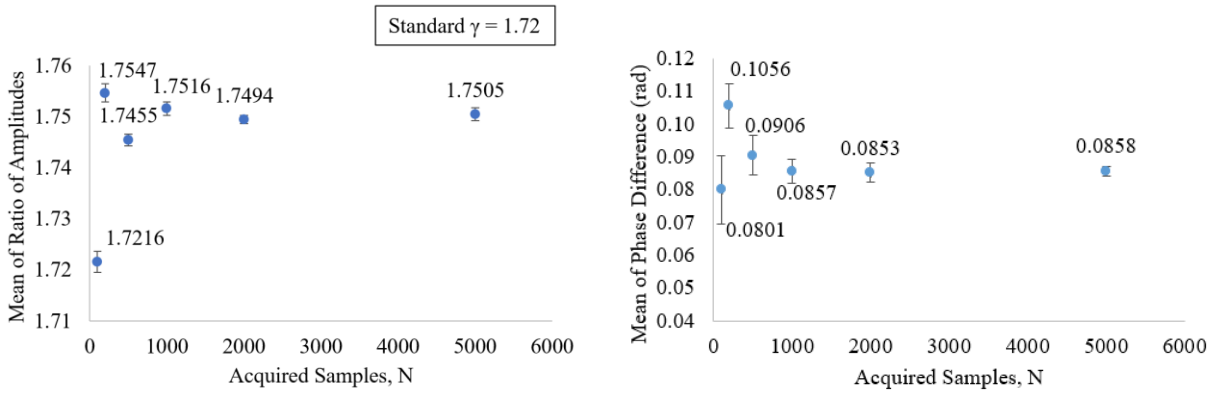

Figure 3.12. Mean of ratio of amplitudes and phase difference for Z_{86}.

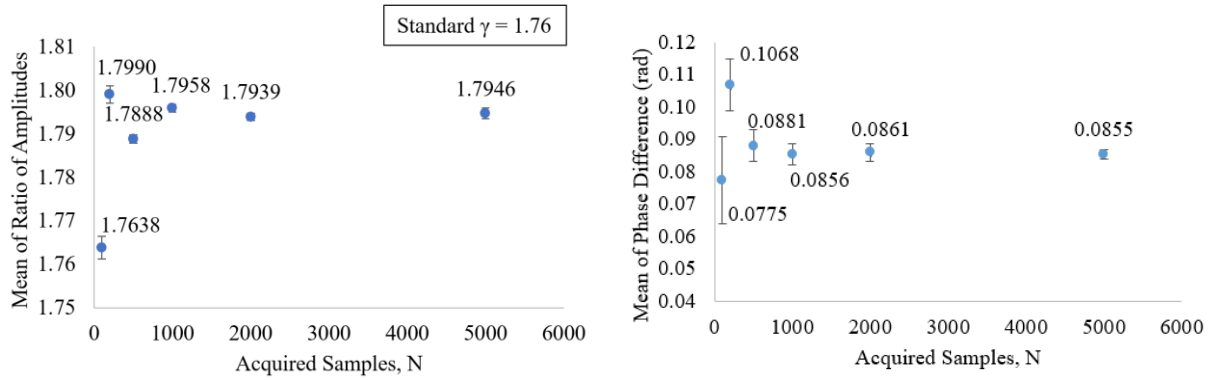

Figure 3.13. Mean of ratio of amplitudes and phase difference for Z_{88}.

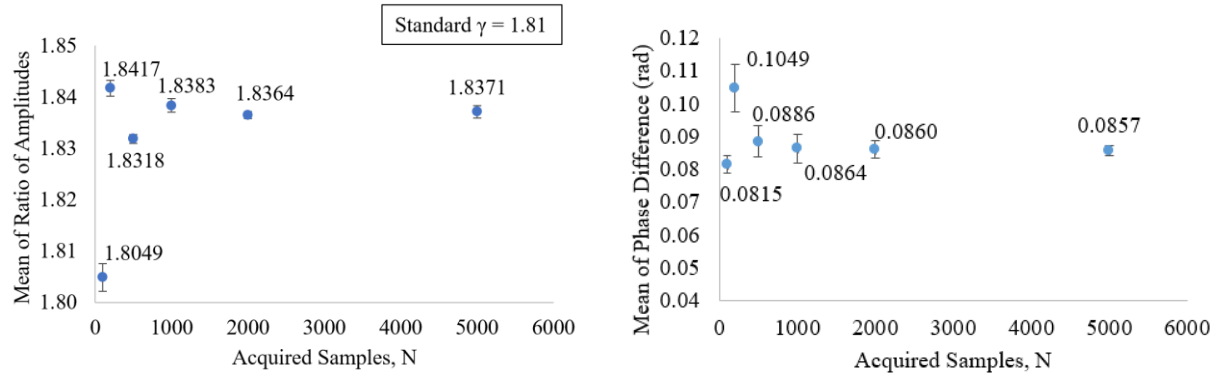

Figure 3.14. Mean of ratio of amplitudes and phase difference for Z_{90}.

Table 3.2 shows the comparison between the test circuit impedance and measured impedance. For all nine measurements, the average percentage of error in measured impedance ranged from 1.26% to 1.67%.

Table 3.2. Comparison between Test Circuit Impedance and Measured Impedance (Averaged Over Six Different Number of Samples, N).

Denote	Test Circuit Impedance (Ω)	Measured Impedance (Ω)	Avg. Error (%)
Z_{74}	74.05	75.17	1.51
Z_{76}	75.95	77.16	1.59
Z_{78}	77.78	79.03	1.61
Z_{80}	80.22	81.47	1.56
Z_{82}	81.81	82.84	1.26
Z_{84}	83.56	84.85	1.54
Z_{86}	86.06	87.28	1.42
Z_{88}	88.21	89.48	1.44
Z_{90}	90.34	91.85	1.67

Table 3.3 shows the calculated average percentage of error in ECF volume (V_{ECF}) based on the error in measured impedance obtained from Table 3.2. Considering the average height of 161.50 cm and the average weight of 76.40 kg for American women of 20 years and older [50], [51], the calculated average percentage of error in measured ECF volume ranged from 0.83% to 1.10%.

Table 3.3. Percentage of Error in Measured ECF Volume based on Error in Measured Impedance.

Denote	Avg. Error in Measured Impedance (%)	Avg. Error in Measured ECF Volume (%)
Z_{74}	1.51	0.99
Z_{76}	1.59	1.05
Z_{78}	1.61	1.06
Z_{80}	1.56	1.03
Z_{82}	1.26	0.83
Z_{84}	1.54	1.01
Z_{86}	1.42	0.94
Z_{88}	1.44	0.95
Z_{90}	1.67	1.10

3.3.2. Multi frequency Impedance Measurement

Figure 3.15 shows the Nyquist plot obtained from both the prototype BIS circuit and the LCR meter at room temperature (72 F) for frequencies in the following set:

$$f = \{100, 500, 1k, 5k, 10k, 20k, 40k, 60k, 80k, 100k\}\ \text{Hz}$$

As the frequency increased (counter-clockwise direction), the real and imaginary parts (resistance and reactance) of the output signal resulted a semi-circular shape.

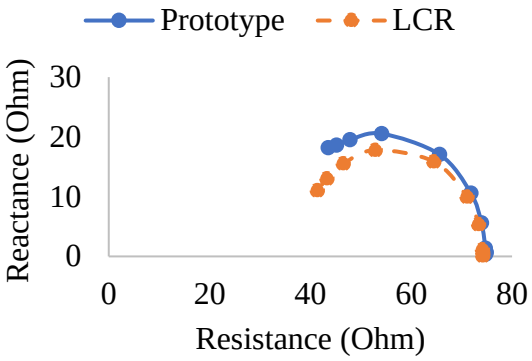

(a) Nyquist plot obtained for Z_{74}.

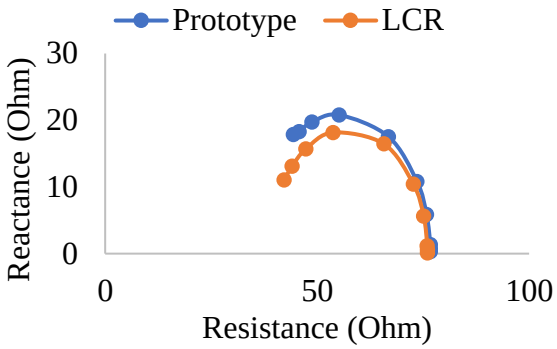

(b) Nyquist plot obtained for Z_{76}.

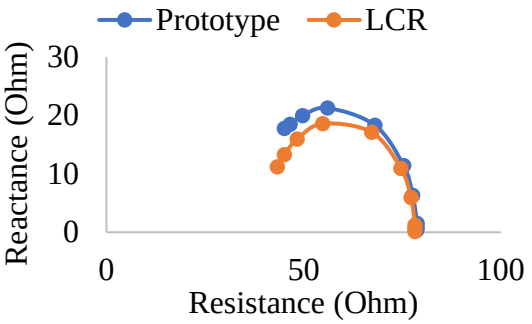

(c) Nyquist plot obtained for Z_{78}.

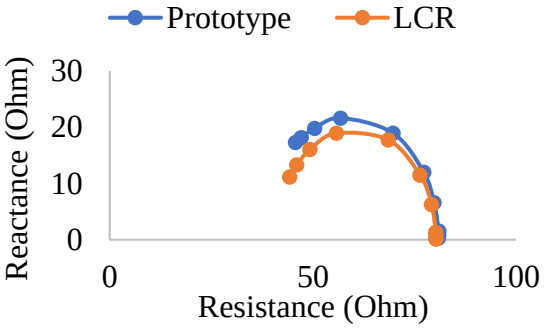

(d) Nyquist plot obtained for Z_{80}.

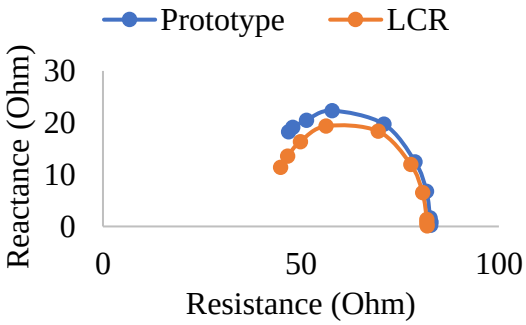

(e) Nyquist plot obtained for Z_{82}.

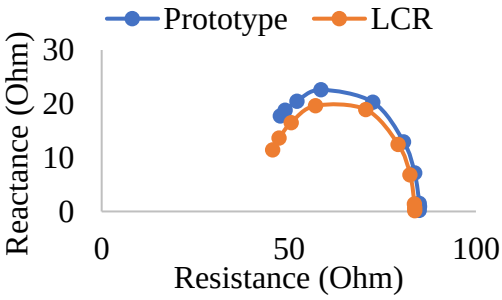

(f) Nyquist plot obtained for Z_{84}.

(figure cont'd)

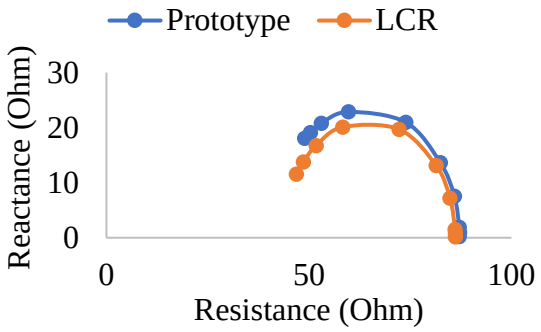

(g) Nyquist plot obtained for Z_{86}.

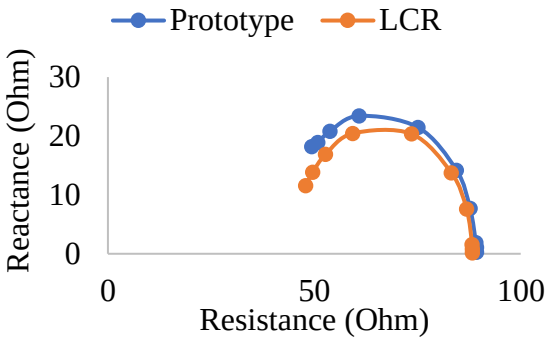

(h) Nyquist plot obtained for Z_{88}.

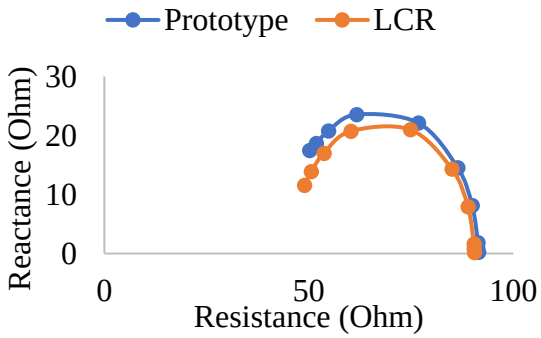

(i) Nyquist plot obtained for Z_{90}.

Figure 3.15. Nyquist plot obtained from prototype BIA measurements and LCR meter measurements for nine test circuit impedance values (Z_{74} to Z_{90}). The frequency increased from 100 Hz to 100 kHz in a counter-clockwise direction.

Figure 3.16 shows the magnitude ratio (m) between the prototype BIA measurements and the LCR meter measurements for nine test circuit impedance (I_{74} to I_{90}) over the frequency range $f = \{100, 500, 1\text{k}, 5\text{k}, 10\text{k}, 20\text{k}, 40\text{k}, 60\text{k}, 80\text{k}, 100\text{k}\}$ Hz. It was observed that on an average, the test circuit impedance obtained from BIA measurements was 1.03 times higher than that of the LCR meter.

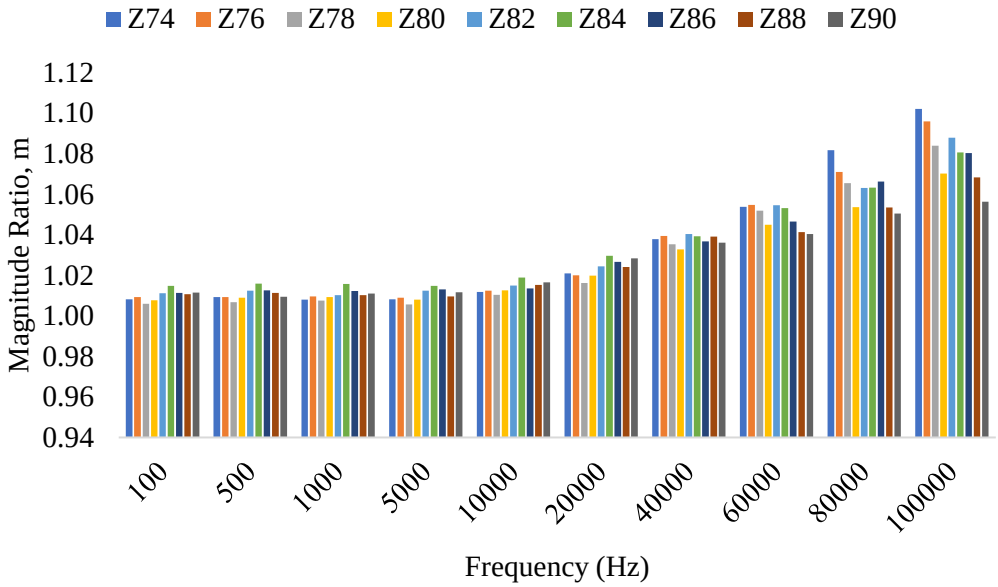

Figure 3.16. Magnitude ratio of test circuit impedance obtained from prototype BIA measurements and LCR meter measurements over the frequency range $f = \{100, 500, 1k, 5k, 10k, 20k, 40k, 60k, 80k, 100k\}$ Hz.

The Nyquist plots obtained for test circuit impedance of 74 Ω (Z74) at temperatures $T = \{72, 75, 80, 85, 90\}$ F are presented in Figure 3.17. For a total of five temperature values including the room temperature of 72 F, no significant changes in Nyquist plots were observed.

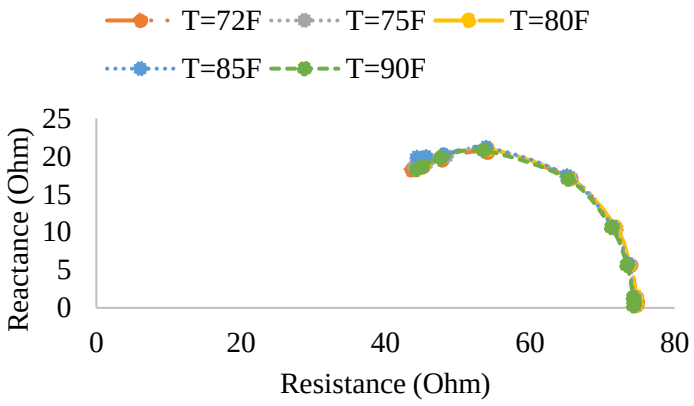

Figure 3.17. Nyquist plots obtained for test circuit impedance, Z_{74} at five different temperature values.

3.4. Battery Life and Number of Compression Cycles

Table 3.4 shows the average power draw by the compression subsystem over one compression cycle of 180 seconds. An average current draw of 246 mA was measured over one compression cycle. For a 5 V supply voltage, an average power draw of 1230 mW was calculated.

Table 3.4. Calculation of Average Power Draw by Compression Subsystem over One Compression Cycle (180 Seconds).

	Phase 1	Phase 2	Phase 3	Phase 4
Avg. Current Draw (mA)	108	177	246	315
Duration (seconds)	30	30	30	90
Avg. Current Draw over One Cycle (mA)	246			
Supply Voltage (V)	5			
Avg. Power Draw over One Cycle (mW)	1230			

Table 3.5 shows the average power draw by the BIA subsystem. An average current draw of 112 mA by all three components was measured for one compression cycle. For a 5 V supply voltage, an average power draw of 560 mW was calculated.

Table 3.5. Calculation of Average Power Draw by BIA Subsystem over One Compression Cycle (180 Seconds).

	Component	Avg. Current Draw over One Cycle (mA)
BIA Subsystem	Arduino Board	50

(table cont'd)

	Component	Avg. Current Draw over One Cycle (mA)
BIA Subsystem	Microcontroller	12
	Howland Circuit	50
Avg. Current Draw over One Cycle by All Components (mA)		112
Supply Voltage (V)		5
Avg. Power Draw over One Cycle (mW)		560

Table 3.6 shows the approximate battery life of the Zeee 5200 mAh 7.4 V battery. The battery life of 21.4 hours was calculated based on the total average power draw by the compression and the BIA subsystem for one full compression cycle. Based on the total battery life and duration of one compression cycle, a total of 429 compression cycles can be achieved.

Table 3.6. Calculation of Battery Life and Number of Compression Cycles.

Total Avg. Power Draw over One Compression Cycle (mW)	1790
Battery Capacity (mWh)	38480
Battery Life (h)	21.4
Total Number of Compression Cycles	429

CHAPTER 4. DISCUSSION

4.1. LYMPHATIC SYSTEM

The relationship between the maximum active tension (M) and flow rate (Q_5) obtained from simulation of the lymphangion chain network agreed with the work of Bertram et. al [32]. For a constant external pressure (p_e), as the maximum active tension decreased, the flow rate reduced. However, it was observed that under the application of an additional variable external pressure indicating a typical pneumatic compression treatment sequence, the peak flow rate increased by 19%. Hence, the application of sequential compression provided by pneumatic pumps is likely to enhance the lymphatic flow for a damaged lymphatic system.

4.2. COMPRESSION SUBSYSTEM

It was observed that the small pneumatic pumps selected, which are of suitable size for a fully portable device, could provide the pressure required during a timeframe that is reasonable and comparable to sequential compression routines in commercially available devices [52]. For a treatment duration of 180 seconds, pressure as high as 54 mmHg, which is greater than what is typically needed, was obtained. It was observed that once reached, the maximum pressure was maintained by all four chambers for the rest of the simulated treatment protocol. The average time required by the chambers (75 seconds) to reach maximum pressure allowed a steady inflation.

However, the voltage vs pressure data for the chambers suggested that the voltage input may not be a reliable way to determine the applied pneumatic pressure provided by small pumps, although the pressures were much more consistent at 5 V than at other voltages. A potential

solution to this problem is the addition of pressure sensors and a feedback control system to regulate the applied pressure during compression therapy.

Duration of treatment could be varied as required through programming of the on-time and off-time of each pump. This would allow adjustments of the inflation time for each chamber [53]. The number of compression cycles can be determined based on the treatment duration and recommended hours of treatment per day. Presumably a physician or licensed therapist would determine the treatment plan in conjunction with the available scientific evidence. A more localized compression can be achieved by increasing the number of chambers and changing their configurations [54]. However, assessment should be made for each individual to determine the pressure level for the chambers [22].

The heat sealable coated nylon fabric showed no signs of wear and tear after multiple tests. This makes the material a good candidate for use as compression chambers. No air leakage was observed during the experiments, suggesting that an impulse sealer is an effective tool for manufacturing the air chambers.

4.3. BIA SUBSYSTEM

The measured impedance obtained by multiplying the ratio of amplitude (γ) and reference impedance (50 Ω) was close to the test circuit impedance. The range for average percentage of error in measured impedance (1.26% to 1.67%) provided an expected error range of 0.83% to 1.10% in ECF volume [refer to equation (5)]. Hence a the BIA subsystem should be sensitive enough to detect a 3% change in ECF volume which is an indication of swelling in a lymphedema affected arm [41]. The Nyquist plots obtained from the oscilloscope for frequency range $f = \{100, 500, 1k, 5k, 10k, 20k, 40k, 60k, 80k, 100k\}$ Hz matched with the ones obtained

from the LCR meter. For lower frequencies (100 Hz to 10 kHz), the average magnitude ratio (the ratio of test circuit impedance between prototype BIA measurements and LCR meter measurements) of was around 1.01. However, as the frequency increased (from 20 kHz to 100 kHz), the magnitude ratio went up. At 100 kHz, the average magnitude ratio was around 1.08. This suggests that the Nyquist plot obtained by the oscilloscope have a slightly larger deviation from the plot obtained by the LCR meter at higher frequencies. No significant changes in Nyquist plots were observed at $T = \{72, 75, 80, 85, 90\}$ F for test circuit impedance of 74 Ω (Z_{74}). This suggests that the BIA circuit should work properly within a temperature range of 72 F to 90 F.

From the Nyquist plots it was observed that the impedance decreases with increasing frequency. This is consistent with the theory since the high-frequency current passes directly through the cell membranes and hence take a shorter route. The plot can provide information on total body water (TBW), extra-cellular fluid (ECF), and tissue mass. In particular, because the ECF measurement is a known diagnostic signal for lymphedema [55], it can serve as a useful signal for feedback control. The data can be made accessible through a wireless connection in future work.

4.4. Battery Life and Portability

It was observed that the Zeee 5200 mAh 7.4 V battery has an approximate battery life of 21.4 hours for the integrated compression and BIS system. Considering a daily compression treatment for 45 minutes [22], each battery can last up to 28 days. It was observed that a total of 429 compression cycles (180 seconds for each compression cycle) can be achieved with the

battery. However, the duration of each compression cycle is likely to vary based on individual needs prescribed by their physicians.

The compression system carrying the pumps, circuit, and battery is sized to fit in a fanny pack that goes around the waist of the person, Figure 4.1. This is likely to enhance mobility by allowing freedom of movement. The lightweight, wearable sleeve is also expected to provide greater comfort, in comparison to the more rigid materials of traditional compression garments, during the course of the treatment. However, some precautions should be taken as the mobility of the arm undergoing compression could be affected while the sleeve is pressurized, potentially increasing the risk of some activities (e.g. preparing food with a knife, carrying a lit candle, etc.).

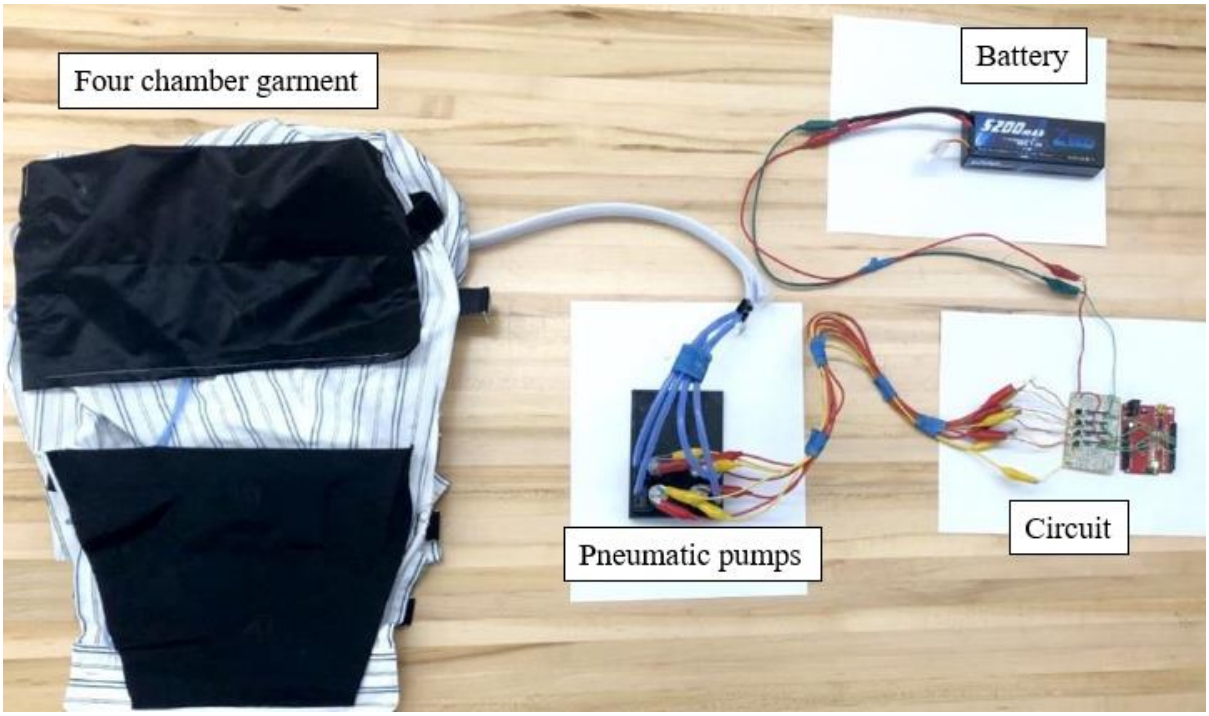

Figure 4.1. Pneumatic compression system carrying pumps, circuit, and portable battery.

CHAPTER 5. CONCLUSION

The prototyping efforts aimed at producing a smart, portable, mechatronic compression system for treatment of lymphedema were described. A lymphatic system with four lymphangion chain network was simulated to observe changes in flow rate for different values of maximum active tension in lymphatic muscles and external pressure. Small battery-operated pneumatic pumps were tested and determined to provide the required pressure and flow rate for pneumatic compression therapy. A heat sealable, polymer-coated nylon fabric was selected and used to construct a compression therapy sleeve for the prototype. A BIA system was built and tested on phantom electrical models of the human arm varying in a manner consistent with the variation in electrical properties during swelling. The microcontroller-based single frequency BIA system was designed to obtain complex impedance measurements of the arm through a non-invasive interface. A benchtop LCR meter validated the measurements to be within the permissible range for detection of changes in arm volume. In the multi frequency BIA system, the frequency and phase responses of the phantom test circuit were characterized by Nyquist plots with real (resistance) and imaginary (reactance) parts of impedance at varying waveform frequencies. The Nyquist plots obtained for different test circuit impedance values were validated by a calibrated LCR meter. For a temperature range of 75 F to 90 F, the BIA circuit can provide accurate measurements of impedance.

For the integrated compression and BIA system, the Zeee 5200 mAh 7.4 V battery can run up to 28 days with a daily compression treatment for 45 minutes. From a packaging standpoint, the integrated compression sleeve could either be worn as an over-garment or be specially designed into ‘lymphedema shirts’ (or pants for lower extremity), eliminating the need to wear any additional garments. Combined with microprocessor-based sensing system and

control algorithms, the finished prototype should be lightweight and portable. The technology can provide freedom of movement and reduce the discomfort associated with current devices. Thus, the future work could lead to an “all-in-one” solution for pneumatic compression treatment for lymphedema.

CHAPTER 6. FUTURE WORK

The present design has some aspects that need further improvement for future studies. For instance, in the design of lymphatic system only the maximum active tension and external pressure were varied to observe the changes in lymph flow. However, that is not the case in an actual lymphatic system. There are other time-dependent variables like the length and diameter of each lymphangion, transmural pressure, and contraction frequency that are present in the system and can affect the lymph flow rate. Hence, a more detailed study of the lymphatic system simulation is needed, taking into consideration the all of these other variables. A complete lymphatic network system can eventually be modeled for upper and lower extremity of the body prior to developing a pneumatic compression device. The will determine the suitable pressure range for compression treatment of each individual.

The proposed compression subsystem used the voltage input obtained from voltage vs pressure data for regulation of pressure in the compression chambers. However, a more reliable way would be the use of pressure sensors as the method of regulating pressure provided by the pneumatic pumps. This will also allow monitoring the changes in extra-cellular fluid (ECF) volume to detect swelling. However, as mentioned earlier, the level of ECF volume that can indicate swelling is likely to vary in every individual. Hence, an initial assessment of body composition is required to obtain information on parameters like total body water (TBW) and intra-cellular fluid (ICF) based on a ‘non-lymphedema’ control.

Enough data may eventually be accumulated to enable the application of dynamic systems feedback control with the human as part of the controlled plant, therefore enabling a precision medicine approach [56] to the management of lymphedema, Figure 6.1. Adaptive

control laws or learning-based controllers may be applied to this human-in-the-loop system that can optimally manage the prescription of treatment.

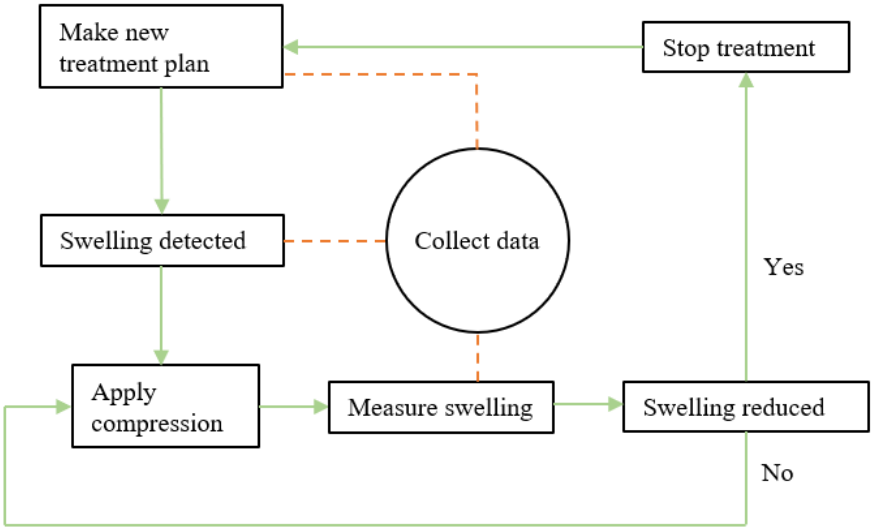

Figure 6.1. Flow chart of proposed integrated device based on feedback control system.

The finished product should be a single compression unit carrying the compression sleeve, microcontroller, pneumatic pumps, and pressure sensors, Figure 6.2. The pumps will start operating upon the detection of swelling. Once the swelling goes down, sensors will detect the reduction and the pumps will stop.

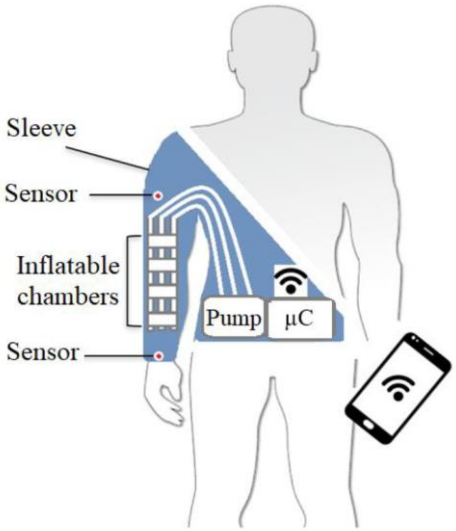

Figure 6.2. Schematic of a potential smart pneumatic compression device.

APPENDIX A. SIMULINK MODEL FOR LYMPHANGION CHAIN NETWORK

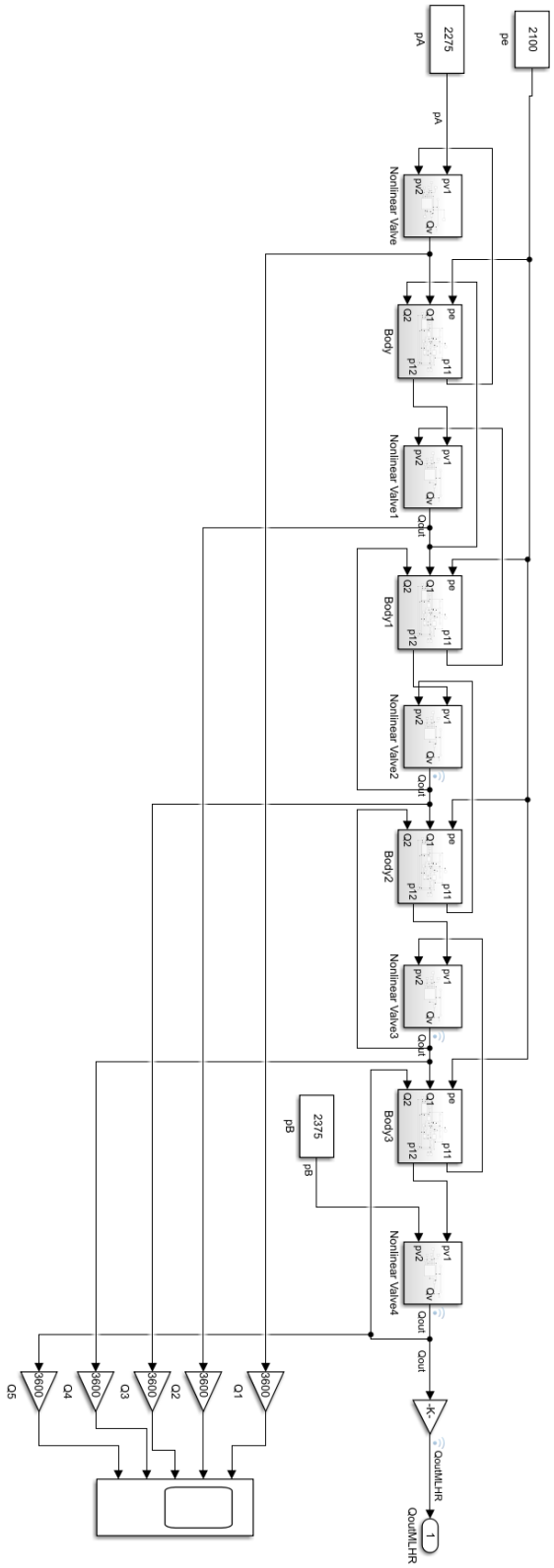

APPENDIX B. ARDUINO CODE FOR SEQUENTIAL OPERATION OF PUMPS

```
int motor1Speed = 200;
int motor2Speed = 200;
int motor3Speed = 200;
int motor4Speed = 200;
int motorPin1 = 6;
int motorPin2 = 9;
int motorPin3 = 10;
int motorPin4 = 11;
long int stop1;
long int stop2;
long int stop3;
long int stop4;
void setup() {
  stop1=millis()+30000;  // n seconds
  stop2=millis()+60000;  // n seconds
  stop3=millis()+90000;  // n seconds
  stop4=millis()+120000;  // n seconds
}
void loop() {
  if (millis()<stop1) {
     analogWrite(motorPin1, motor1Speed);
  } else {
     analogWrite(motorPin1, motor1Speed);
  if (millis()<stop2) {
     analogWrite(motorPin2, motor2Speed);
  } else {
     analogWrite(motorPin2, motor2Speed);
if (millis()<stop3) {
     analogWrite(motorPin3, motor3Speed);
  } else {
     analogWrite(motorPin3, motor3Speed);
     if (millis()<stop4) {
     analogWrite(motorPin4, motor4Speed);
  } else {
     analogWrite(motorPin4, motor4Speed);
if (millis()>stop4) {
     analogWrite(motorPin1, 0);
     analogWrite(motorPin2, 0);
     analogWrite(motorPin3, 0);
     analogWrite(motorPin4, 0);
  }
}
}
}}
```

APPENDIX C. ARDUINO CODE FOR SINGLE FREQUENCY IMPEDANCE MEASUREMENT

```
//from http://sphinx.mythic-beasts.com/~markt/ATmega-timers.html
//The 16 modes are summarized in this table.
//code  Mode   TOP    Update of OCR1x      TOV1 Flag Set
//0       Normal          0xFFFF          Immediate       MAX
//1       PWM, Phase Correct, 8-bit    0x00FF          TOP    BOTTOM
//2       PWM, Phase Correct, 9-bit    0x01FF          TOP    BOTTOM
//3       PWM, Phase Correct, 10-bit  0x03FF          TOP    BOTTOM
//4       CTC    OCR1A          Immediate       MAX
//5       Fast PWM, 8-bit         0x00FF          BOTTOM       TOP
//6       Fast PWM, 9-bit         0x01FF          BOTTOM       TOP
//7       Fast PWM, 10-bit        0x03FF          BOTTOM       TOP
//8       PWM, Phase and Frequency Correct  ICR1   BOTTOM       BOTTOM
//9       PWM, Phase and Frequency Correct  OCR1A          BOTTOM       BOTTOM
//10      PWM, Phase Correct  ICR1   TOP    BOTTOM
//11      PWM, Phase Correct  OCR1A          TOP    BOTTOM
//12      CTC    ICR1   Immediate       MAX
//13      (Reserved)      -         -         -
//14      Fast PWM       ICR1   BOTTOM       TOP
//15      Fast PWM       OCR1A          BOTTOM       TOP

//Note that in PWM, Phase and Frequency Correct mode (8), the PWM frequency
// is calculated by
// f_clk / (2 * N * TOP )
// where N is the prescaler value and TOP is the timer/counter top set in ICR1
//
void timer1_setup (byte mode, int prescale, byte outmode_A, byte outmode_B, byte
capture_mode)
{
  // enforce field widths for sanity
  mode &= 15 ;
  outmode_A &= 3 ;
  outmode_B &= 3 ;
  capture_mode &= 3 ;

  byte clock_mode = 0 ; // 0 means no clocking - the counter is frozen.
  switch (prescale)
  {
    case 1: clock_mode = 1 ; break ;
    case 8: clock_mode = 2 ; break ;
    case 64: clock_mode = 3 ; break ;
    case 256: clock_mode = 4 ; break ;
    case 1024: clock_mode = 5 ; break ;
    default:
      if (prescale < 0)
```

```
      clock_mode = 7 ; // external clock
  }
  TCCR1A = (outmode_A << 6) | (outmode_B << 4) | (mode & 3) ;
  TCCR1B = (capture_mode << 6) | ((mode & 0xC) << 1) | clock_mode ;
}

void setup() {
        // put your setup code here, to run once:
        pinMode(9, OUTPUT);
  pinMode(A0, INPUT);
  pinMode(A1, INPUT);
        Serial.begin(19200);
}

//Each time through the loop, we will calculate the Fourier coefficient once
// Assume a signal frequency of 100 Hz, and a sampling frequency of 500 Hz.
// Then the Fourier coefficient can be calculated over 2 cycles using N=1000 samples
//
//
void loop() {
        // put your main code here, to run repeatedly:
        //First we need to output a 100 Hz signal

        /* Code to output approximately a 100 Hz signal using Timer/Counter 1 on pin 9 */
        timer1_setup(0, 0, 0, 0, 0);
        ICR1 = 1024; //results in just over 10 bit pwm resolution and frequency of 122.0703125
Hz
        OCR1A = 512; //results in 50% duty cycle signal on pin 9
  TCNT1=0;
        timer1_setup(8, 64, 2, 0, 0);
        //PWM Output will appear on pin 9 (OC1A)

        /* Now collect the correct number of samples and calculate
        the Fourier coefficients of analog A0 and A1 using
        a rolling sum */
        long i = 0; //sample number
        long N = 1000; //Number of samples to acquire
        long dt = 2500; //microseconds per sample
        int chA0, chA1; //values to hold analog samples
        _Accum chA0k, chA1k; //fixed point conversions of analog samples

        _Accum Real0, Imag0, Real1, Imag1, Real2, Imag2;
        Real1 = itok(0);
        Imag1 = itok(0);
        Real0 = itok(0);
        Imag0 = itok(0);
```

```
        _Accum cosvk, sinvk;
        _Accum phase = 0;
        _Accum dphase = ftok( 2*3.14159265358979*122.0703125*0.0025 );

        long lastt = micros();
        long t = micros();

        //we need to collect N samples
        for (int i = 0; i < N; ++i )
        {
                while ((t = micros())-lastt < dt) {} //wait for the next sample time by doing
nothing
                //collect the samples (as close to synchronous as possible)
                chA0 = analogRead(A0); //range 0-1023
                chA1 = analogRead(A1); //range 0-1023

                //convert the measurements to fixed point
                chA0k = itok(chA0);
                chA1k = itok(chA1);

                //update the phase angle of the transform
                phase = phase + dphase; //fixed point arithmetic, phase update

                //now calculate the sincos coefficients
                sinvk = sincosk( phase, &cosvk ); //get the trig values

                //calculate coefficients in recurrence relation
                _Accum C1, C2;
                C1 = divkD( itok(i), itok(i+1) );
                C2 = divkD( itok(2), itok(i+1) );

                Real0 = mulkD(Real0, C1) + mulkD( mulkD(cosvk, chA0k), C2 );
                Imag0 = mulkD(Imag0, C1) + mulkD( mulkD(sinvk, chA0k), C2 );

                Real1 = mulkD(Real1, C1) + mulkD( mulkD(cosvk, chA1k), C2 );
                Imag1 = mulkD(Imag1, C1) + mulkD( mulkD(sinvk, chA1k), C2 );

                lastt = t;  //update the last loop timestamp
        }
        //At this point Real0 + i*Imag0 is the fourier coefficient of chA0 samples
        //            Real1 + i*Imag1 is the fourier coefficient of chA1 samples

        Serial.println("Values (Real0, Imag0, Real1, Imag1)");
        Serial.println(ktod(Real0),5);
        Serial.println(ktod(Imag0),5);
        Serial.println(ktod(Real1),5);
```

```
        Serial.println(ktod(Imag1),5);

        Serial.println();
        delay(1000);
}
```

REFERENCES

[1] S. G. Rockson, "Lymphedema," *Vasc. Med. (United Kingdom)*, vol. 21, no. 1, pp. 77–81, 2016.

[2] V. Velanovich and W. Szymanski, "Quality of life of breast cancer patients with lymphedema," *Am. J. Surg.*, vol. 177, no. 3, pp. 184–188, 1999.

[3] M. B. Tobin, H. J. Lacey, L. Meyer, and P. S. Mortimer, "The psychological morbidity of breast cancer–related arm swelling. Psychological morbidity of lymphoedema," *Cancer*, vol. 72, no. 11, pp. 3248–3252, 1993.

[4] R. H. Zeissler, G. B. Rose, and P. A. Nelson, "Postmastectomy lymphedema: late results of treatment in 385 patients.," *Arch. Phys. Med. Rehabil.*, vol. 53, no. 4, pp. 159–166, 1972.

[5] K. E. Rose, H. M. Taylor, and R. G. Twycross, "Long-term compliance with treatment in obstructive arm lymphoedema in cancer," *Palliat. Med.*, vol. 5, no. 1, pp. 52–55, 1991.

[6] OpenStax College, *Anatomy and Physiology*. 2013.

[7] L. Sherwood, "Human physiology from cells to systems Ninth Edition," *Appetite*. Cengage Learning, 2016.

[8] S. Jamalian, M. J. Davis, D. C. Zawieja, and J. E. Moore, "Network Scale Modeling of Lymph Transport and Its Effective Pumping Parameters," *PLoS One*, vol. 11, no. 2, 2016.

[9] R. M. Morrell, M. Y. Halyard, S. E. Schild, M. S. Ali, L. L. Gunderson, and B. A. Pockaj, "Breast cancer-related lymphedema," *Mayo Clinic Proceedings*. Elsevier, pp. 1480–1484, 2005.

[10] A. K. Greene, "Epidemiology and morbidity of lymphedema," in *Lymphedema: Presentation, Diagnosis, and Treatment*, Springer, Cham, 2015, pp. 33–44.

[11] K. Segerström, P. Bjerle, S. Graffman, and A. Nyström, "Factors that influence the incidence of brachial oedema after treatment of breast cancer," *Scand. J. Plast. Reconstr. Surg. Hand Surg.*, vol. 26, no. 2, pp. 223–227, 1992.

[12] R. H. Rönkä, M. S. Pamilo, K. A. J. Von Smitten, and M. H. K. Leidenius, "Breast lymphedema after breast conserving treatment," *Acta Oncol. (Madr).*, vol. 43, no. 6, pp. 551–557, 2004.

[13] M. R. Fu *et al.*, "L-Dex ratio in detecting breast cancer-related lymphedema: Reliability, sensitivity, and specificity," *Lymphology*, vol. 46, no. 2, pp. 85–96, 2013.

[14] S. F. Khalil, M. S. Mohktar, and F. Ibrahim, "The theory and fundamentals of bioimpedance analysis in clinical status monitoring and diagnosis of diseases," *Sensors (Switzerland)*, vol. 14, no. 6, pp. 10895–10928, 2014.

[15] J. M. Armer, J. M. Hulett, M. Bernas, P. Ostby, B. R. Stewart, and J. N. Cormier, "Best-

practice guidelines in assessment, risk reduction, management, and surveillance for post-breast cancer lymphedema," *Curr. Breast Cancer Rep.*, vol. 5, no. 2, pp. 134–144, 2013.

[16] D. S. C. Ko, R. Lerner, G. Klose, and A. B. Cosimi, "Effective treatment of lymphedema of the extremities," *Arch. Surg.*, vol. 133, no. 4, pp. 452–458, 1998.

[17] S. Buragadda, A. A. Alhusaini, G. R. Melam, and N. Arora, "Effect of complete decongestive therapy and a home program for patients with post mastectomy lymphedema," *J. Phys. Ther. Sci.*, vol. 27, no. 9, pp. 2743–2748, 2015.

[18] J. L. Feldman, N. L. Stout, A. Wanchai, B. R. Stewart, J. N. Cormier, and J. M. Armer, "Intermittent pneumatic compression therapy: A systematic review," *Lymphology*, vol. 45, no. 1, pp. 13–25, 2012.

[19] J. J. Phillips and S. J. Gordon, "Intermittent pneumatic compression dosage for adults and children with lymphedema: A systematic review," *Lymphat. Res. Biol.*, vol. 17, pp. 2–18, 2019.

[20] M. Zaleska *et al.*, "Pressures and timing of intermittent pneumatic compression devices for efficient tissue fluid and lymph flow in limbs with Lymphedema," *Lymphat. Res. Biol.*, vol. 11, no. 4, pp. 227–232, 2013.

[21] Centers for Medicare & Medicaid Services, "Local Coverage Determination (LCD): Pneumatic Compression Devices (L33829)." [Online]. Available: https://www.cms.gov/medicare-coverage-database/details/lcd-details.aspx?LCDId=33829&ver=42&Date=&DocID=L33829&bc=iAAAAAIAAAAA&.

[22] M. Zaleska, W. L. Olszewski, and M. Durlik, "The effectiveness of intermittent pneumatic compression in long-term therapy of lymphedema of lower limbs," *Lymphat. Res. Biol.*, vol. 12, no. 2, pp. 103–109, 2014.

[23] Bio Compression Systems Inc., "Model SC-3004 Sequential Circulator." [Online]. Available: https://www.biocompression.com/model-sc-3004-sequential-circulator/.

[24] R. Scheer, "Compression garments for managing lymphoedema," *J. Lymphoedema*, vol. 12, no. 1, pp. 39–45, 2017.

[25] Y. Xiong and X. Tao, "Compression garments for medical therapy and sports," *Polymers (Basel).*, vol. 10, no. 6, p. 663, 2018.

[26] Impedimed, "Bioimpedance spectroscopy (BIS) technology." [Online]. Available: https://www.impedimed.com/healthcare/bis-technology/.

[27] K. E. Adams *et al.*, "Direct evidence of lymphatic function improvement after advanced pneumatic compression device treatment of lymphedema," *Biomed. Opt. Express*, vol. 1, no. 1, p. 114, 2010.

[28] S. Muluk and E. Taffe, "A Review of Pneumatic Compression Therapy in the Treatment of Lymphedema," *SM Vasc Med.*, vol. 1, no. 1, p. 1003, 2016.

[29] G. Pettinico and G. R. Milne, “Living by the numbers: understanding the ‘quantification effect,’” *J. Consum. Mark.*, 2017.

[30] N. P. Reddy, T. A. Krouskop, and P. H. Newell, “A computer model of the lymphatic system,” *Comput. Biol. Med.*, vol. 7, no. 3, pp. 181–197, 1977.

[31] R. E. Drake, S. J. Allen, J. Katz, J. C. Gabel, and G. A. Laine, “Equivalent circuit technique for lymph flow studies,” *Am. J. Physiol. - Hear. Circ. Physiol.*, vol. 251, no. 5, pp. H1090–H1094, 1986.

[32] C. D. Bertram, C. Macaskill, M. J. Davis, and J. E. Moore, “Development of a model of a multi-lymphangion lymphatic vessel incorporating realistic and measured parameter values,” *Biomech. Model. Mechanobiol.*, vol. 13, pp. 401–416, 2014.

[33] U. Pilch, M. Wozniewski, and A. Szuba, “Influence of compression cycle time and number of sleeve chambers on upper extremity lymphedema volume reduction during intermittent pneumatic compression,” *Lymphology*, vol. 42, no. 1, pp. 26–35, 2009.

[34] M. Miguel, M. Leite, A. M. R. Ribeiro, A. M. Deus, L. Reis, and M. F. Vaz, “Failure of polymer coated nylon parts produced by additive manufacturing,” *Eng. Fail. Anal.*, vol. 101, pp. 485–492, 2019.

[35] R. A. Maclellan, *Pneumatic compression*. Springer, Cham, 215AD.

[36] M. F. Cheng, Y. Y. Chen, T. R. Jang, W. L. Lin, J. Chen, and K. C. Hsieh, “Total body composition estimated by standing-posture 8-electrode bioelectrical impedance analysis in male wrestlers,” *Biol. Sport*, vol. 33, no. 4, p. 399, 2016.

[37] B. Ibrahim, D. A. Hall, and R. Jaffari, “Bio-impedance spectroscopy (BIS) measurement system for wearable devices,” in *IEEE Biomedical Circuits and Systems Conference (BioCAS)*, 2017, pp. 1–4.

[38] “Electrical theory behind the measurement of body fluids with bioimpedance spectroscopy (BIS).” [Online]. Available: https://pure.au.dk/portal/files/20320521/lecture_notes_on_bis.pdf.

[39] “500 kHz / 1 MHz Precision LCR Meter.” [Online]. Available: https://bkpmedia.s3.amazonaws.com/downloads/datasheets/en-us/894_895_datasheet.pdf.

[40] M. Y. Jaffrin and H. Morel, “Body fluid volumes measurements by impedance: A review of bioimpedance spectroscopy (BIS) and bioimpedance analysis (BIA) methods,” *Med. Eng. Phys.*, vol. 30, no. 10, pp. 1257–1269, 2008.

[41] L. Kim, J. Y. Jeon, I. Y. Sung, S. Y. Jeong, J. H. Do, and H. J. Kim, “Prediction of Treatment Outcome with Bioimpedance Measurements in Breast Cancer Related Lymphedema Patients,” *Ann. Rehabil. Med.*, vol. 35, no. 5, pp. 687–693, 2011.

[42] H. Yazdanian, M. M. Samani, and A. Mahanm, “Characteristics of the Howland current source for bioelectric impedance measurements systems,” in *2013 20th Iranian Conference on Biomedical Engineering, ICBME 2013*, 2013, pp. 189–193.

[43] Texas Instruments, “INA821 Datasheet.” [Online]. Available: https://www.ti.com/document-viewer/INA821/datasheet/features-sbos7928252#SBOS7928252.

[44] Texas Instruments, “OPA340 Datasheet.” [Online]. Available: https://www.ti.com/document-viewer/OPA340/datasheet.

[45] R. Chandler, G; Denson, W.; Rossi, M.; Wanner, “Failure Mode/Mechanism Distributions,” 1991.

[46] “Arduino Uno Rev3.” [Online]. Available: https://store.arduino.cc/usa/arduino-uno-rev3.

[47] “8-bit AVR Microcontroller with 32K Bytes In-System Programmable Flash.” [Online]. Available: http://ww1.microchip.com/downloads/en/DeviceDoc/Atmel-7810-Automotive-Microcontrollers-ATmega328P_Datasheet.pdf.

[48] A. S. N. Mokhtar, M. I. Ayub, N. Ismail, and N. G. N. Daud, “Implementation of trigonometric function using CORDIC algorithms,” in *AIP Conference Proceedings*, 2018, p. 020040.

[49] W. Elmenreich, M. Rosenblattl, and A. Wolf, “Fixed point library based on ISO/IEC standard DTR 18037 for Atmel AVR microcontrollers,” in *Proceedings of the 5th International Workshop on Intelligent Solutions in Embedded Systems, WISES 07*, 2007, pp. 101–113.

[50] “Average human height by country.” [Online]. Available: https://en.wikipedia.org/wiki/Average_human_height_by_country.

[51] “Human body weight.” [Online]. Available: https://en.wikipedia.org/wiki/Human_body_weight.

[52] Biocompression, “Model SC-2004-OC Sequential Circulator | Bio Compression Systems, Inc.” [Online]. Available: https://www.biocompression.com/model-sc-2004-oc-sequential-circulator/.

[53] M. Zaleska *et al.*, “Pressures and timing of intermittent pneumatic compression devices for efficient tissue fluid and lymph flow in limbs with Lymphedema,” *Lymphat. Res. Biol.*, vol. 11, no. 4, pp. 227–232, 2013.

[54] C. J. Chang and J. N. Cormier, “Lymphedema Interventions: Exercise, Surgery, and Compression Devices,” *Semin. Oncol. Nurs.*, vol. 29, no. 1, pp. 28–40, 2013.

[55] S. Hayes, M. Janda, B. Cornish, D. Battistutta, and B. Newman, “Lymphedema secondary to breast cancer: How choice of measure influences diagnosis, prevalence, and identifiable risk factors,” *Lymphology*, vol. 41, no. 1, pp. 18–28, 2008.

[56] F. S. Collins and H. Varmus, “A new initiative on precision medicine,” *N. Engl. J. Med.*, vol. 372, no. 9, pp. 793–795, 2015.

VITA

Mohammad Imrul Kayes was born in February 1989. He completed his Bachelor's in Mechanical Engineering from Khulna University of Engineering & Technology (Khulna, Bangladesh) in 2012. He obtained his first Masters in Mechanical Engineering from Louisiana Tech University (Ruston, Louisiana, USA) in 2014. He plans to receive his second Masters in May 2021 from Louisiana State University (Baton Rouge, Louisiana, USA). His current research project was funded by the LSU LIFT^2 (Leverage Innovation for Technology Transfer) grant, awarded to his supervisor, Dr. Hunter B Gilbert. The project focused on developing a lymphedema compression device to provide a smart and more convenient option for secondary lymphedema management. As a part of this project, Mohammad Kayes attended the NSF I-CORPS program to learn about commercialization of invented technology. He also attended the 2019 National Lymphedema Network Conference in Boston, Massachusetts as a part of the project. Upon completion of his study, Mohammad Kayes plans to work in a medical device industry.